Thin Solid Films 853 (2026) 141059



Contents lists available at ScienceDirect

Thin Solid Films

journal homepage: www.elsevier.com/locate/tsf



Physics-constrained, Kramers–Kronig-consistent retrieval of the refractive index and thickness of porous silicon thin films from multi-angle reflectance

Guido Mula

PoroSiLab, Dipartimento di Fisica, Università degli Studi di Cagliari, Cittadella Universitaria di Monserrato, S.P. 8 km 0.700, Monserrato, CA, 09042, Italy

ARTICLE INFO

Keywords:
Optical parameters extraction
Thin films
Software
Model-free

ABSTRACT

The retrieval of the optical constants of a thin film from its reflectance becomes demanding when the film is not a homogeneous, flat-interface material, as in porous silicon. There the standard approach, postulating a dielectric model and fitting its parameters, grows less reliable, the residual error increases, and the fit can become time consuming. For such complex materials we propose a change of point of view, representing the refractive index n (λ) directly on a set of nodes constrained only by simple, physics-founded rules rather than by an assumed dielectric model. The method is implemented in a Python code, Ophira (OPtical tHIn-film Reflectance Analyzer), which retrieves $n(\lambda)$ and the thickness d from spectra measured at several incidence angles. The retrieval is constrained only by smoothness, monotonicity in the transparent region and optical-thickness anchoring, and is verified a posteriori through Kramers-Kronig consistency and geometric triangulation. Applied to porous silicon across a range of porosities, including the high-porosity regime where effective-medium and oscillator models struggle, it yields reflectance fits and thicknesses consistent with electron-microscopy cross sections and with an established oscillator-based analysis. Ophira is proposed as a complement to model-based tools, not a replacement.

1. Introduction

The fitting of optical reflectivity spectra is both a challenge and a routine tool in industry and research. For instance, there are industrial tools dedicated to the measurement of thickness [1,2] for standard materials where the only unknown parameter is the thickness. However, complex inhomogeneous materials as Porous Silicon (PSi) [3] are significantly more complex. PSi is a versatile porous material that has been the object of active research in many fields, such as biosensors [4–7], photovoltaics [8–11], magnetic properties [12–14], drug-delivery systems [15–18] and much more. Its versatility rests on the fact that the porosity, and therefore the refractive index, can be tuned over a wide range during the standard electrochemical fabrication, so that thin films, multilayers and Bragg reflectors [19–22], microcavities and rugate filters [23,24] can be produced directly in the silicon substrate [3,25]. This tunability has made PSi particularly attractive for optical devices and, above all, for label-free optical (bio) sensing [26–29], which represents a large fraction of the recent PSi-optics literature. The principle of optical (bio)sensing is that the optical response of PSi is related to the combined optical response of the porous matrix and of the material filling the pores, so that a change in the filling material necessarily implies a change in the optical response. The physical quantity most commonly used to follow such changes is the optical thickness from thin-film interference, and to achieve high sensitivity the standard practice is to detect the variations of the Effective Optical Thickness (EOT) through a Fourier transform of the reflectivity spectra [30–32]. While this is standard physics, the difficulty arises from the fact that PSi is far from being an easy material to model optically and tightly bounded model cannot succeed in fully describing its behavior.

The sensing by means of detecting the modification of EOT is built on the modifications of the complex refractive index, $\tilde{n}(\lambda) = n(\lambda) + ik(\lambda)n(\lambda)$ and $k(\lambda)$, and the layer thickness d induced by some variable modification on the EOT-based sensor. Determining $\tilde{n}(\lambda)$ and $k(\lambda)$ from a measured reflectance spectrum is, however, an ill-posed inverse problem, and it is made harder by the nature of PSi itself. The material is a disordered, high-surface-area network whose optical response is usually modelled with an effective-medium approximation (EMA, e.g. Bruggeman or Maxwell-Garnett models), which maps a porosity to a refractive index [33–36]. EMA works well at moderate porosity, but it rests on

E-mail address: guido.mula@unica.it.

https://doi.org/10.1016/j.tsf.2026.141059
Received 22 July 2026; Received in revised form 1 October 2026; Accepted 21 October 2026
Available online 21 October 2026
0040-6090/© 2026 The Author(s). Published by Elsevier B.V. This is an open access article under the CC BY license (http://creativecommons.org/licenses/by/4.0/).

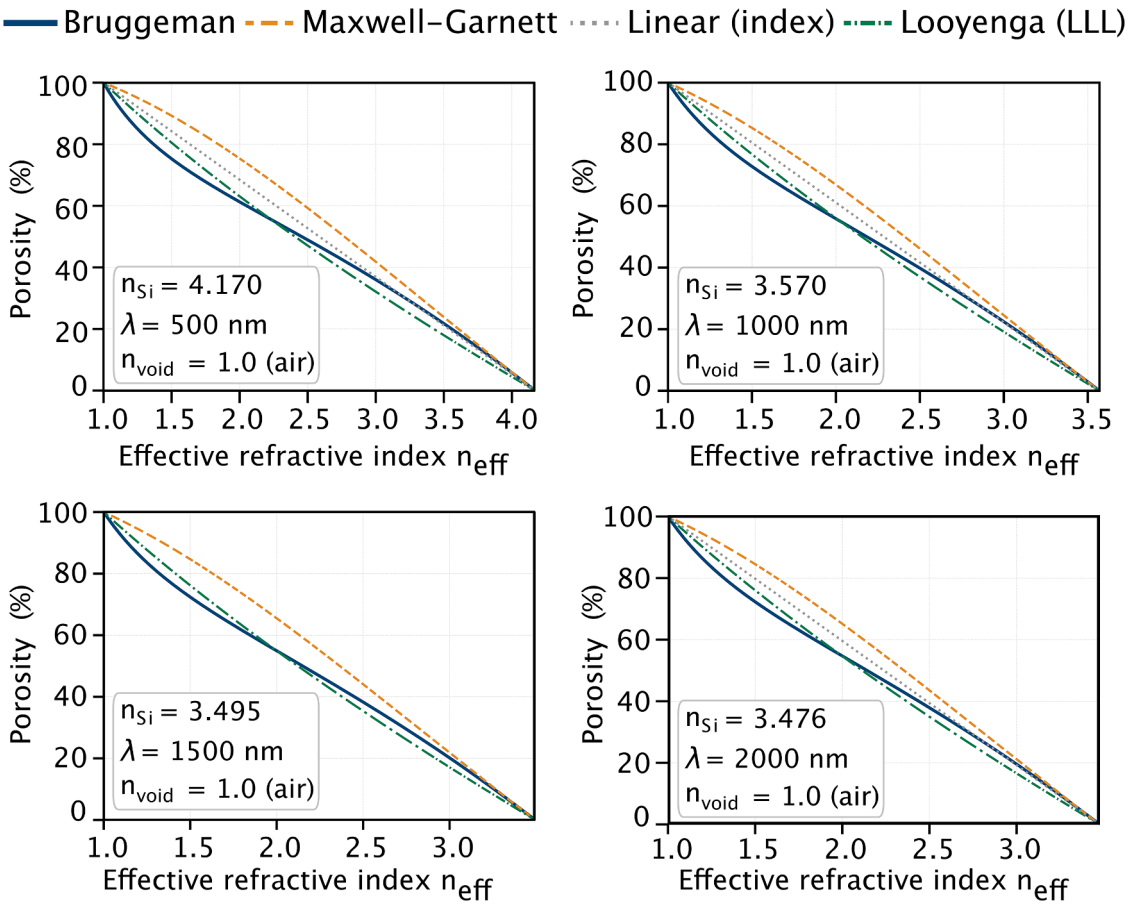


Fig. 1. Porosity inferred from a measured effective refractive index n_{eff} for four effective-medium mixing rules (Bruggeman, Maxwell–Garnett, Looyenga, linear-index), at (a) 500, (b) 1000, (c) 1500 and (d) 2000 nm; the dispersive silicon index n_{Si} is indicated in each panel and $n_{void} = 1$ (air).

assumptions (dilute, well-separated, simply-shaped inclusions) that fail for the highly porous, morphologically complex layers that are of most interest, where the fine structure of the network, not merely its void fraction, controls the optical response [37–39]. The problem is complex because of real-sample effects, as lateral inhomogeneity, gradients and thickness non-uniformity across the probed area, which in turn lead to damping the interference-fringe contrast [40], and by optical anisotropy: PSi is intrinsically anisotropic and its form birefringence has been studied by several authors mainly on its [110] orientation where the ordinary and the extraordinary refractive indexes are orthogonal for a light beam impinging vertically from the surface [41,42]. Already on that orientation, several authors [43] showed that a simple modelling is not enough for the correct description of the origin of the birefringence. Therefore, while EMA models are adequate for several applications, they fail when the observed behavior depends on tiny structural details that cannot be accounted for by averaged methods.

A central difficulty when using the EMA models is that there is no consensus on which mixing rule best represents PSi. Different authors adopt different rules and different inclusion geometries for the same material: Bruggeman with ellipsoidal Si nanoclusters [42,44–46] or the Maxwell–Garnett formula with a cylindrical description of the (100) structure [47] or the Looyenga that assumes a homogenous distribution of the pores within the solid matrix [30,48,49]. Commercial state-of-the-art fitting packages themselves in general offer a choice among several EMA models, which is in itself an admission that no single rule is established as correct. The consequence of this freedom of choice is quantitative and is illustrated in Fig. 1: for a given measured effective refractive index, the porosity inferred from four common mixing rules (Bruggeman, Maxwell–Garnett, Looyenga and a linear-index rule) differs by up to about 12% (reaching ~15% at 500 nm), the disagreement being largest in the high-porosity region that is of greatest interest. Beyond this model-selection ambiguity, there is direct experimental evidence that the averaged approaches do not capture the detailed optical behavior of PSi as for the form birefringence we already cited [42,44–46]. On (100)-oriented PSi, positive form birefringence would be expected from those earlier results, yet a negative birefringence has recently been demonstrated by G. Mula et al. [50], a behavior that the averaged models proposed in the literature do not account for. Using an EMA description, therefore, gives a reasonable phenomenological account but does not guarantee that the resulting interpretation is the best-fitting or the only possible one.

For these reasons, the extraction of the optical constants from reflectance is itself the critical step. Two broad strategies are used. The first imposes a physical dielectric model, a sum of oscillators (Drude–Lorentz, Tauc–Lorentz) whose parameters are fitted, as implemented in widely used commercial packages [36,51]. Such models are Kramers–Kronig (KK) consistent by construction and give directly interpretable parameters, but they describe a disordered porous film only approximately, and a "perfect" fit is essentially impossible given the inhomogeneities of PSi. This is quantitative: by the default fit-quality classification of a widely used oscillator-modelling package Scout, on page 185 of their technical manual [52] a reflectance-fit deviation above 0.1 is rated "rejected" and a fit must fall below 0.01 to be rated merely "acceptable", while standard, well-characterized materials routinely reach the "good" or "excellent" levels below 0.001. The fits we obtain for high-porosity PSi with this approach most often show deviations in the 0.1 – 0.15 interval, therefore in the "rejected" band and more than an order of magnitude away from "acceptable", even though the reflectance overlay is visually close. An example of this is shown in § 4.3, where a direct comparison of Ophira and Scout fitting results is reported. This



Fig. 2. Main window of Ophira. The upper left part shows the main graphs of the experimental and simulated curves (here they are highly similar and therefore appear superposed), the residues and the ***n*** and ***k*** dispersion curves. On the right are the angle selection/load for the reflectivity spectra. In the central part of the image, all the control sliders are visible, while on the bottom part all the control buttons are visible. The description of the various functions is in the text.

reliability evaluation gap is a direct expression of the mismatch between a discrete-oscillator dielectric and a disordered porous network. The second strategy retains flexibility by representing the dielectric function on a dense basis (variational or spline-based) while enforcing KK consistency during the fit, as in the variational-dielectric-function method [53] and in KK-consistent B-spline parameterizations [54], now available in commercial spectroscopic-analysis software. Ellipsometry provides an independent and powerful multi-angle route to *n*, *k* and *d* and has been applied to PSi [55], but it requires dedicated instrumentation and its own modelling, which is already complex for empty PSi and critically so when a third material is present within the pores.

Meanwhile, much of the sensing literature that uses reflectometric interference (Reflectometric Interference Fourier Transform Spectroscopy/ Reflective interferometric Fourier transform spectroscopy) [56, 57] and related porous-silicon interferometric transducers [58], by design, track the shift of the optical thickness as a highly sensitive transduction signal, an approach extended to other nanostructured interferometric platforms such as TiO_2 nanotube arrays [59], without requiring the full dispersion $n(\lambda)$ to be retrieved. What is missing is a route that keeps the flexibility needed for complex, imperfect films, does not commit to a specific dielectric model a priori, and still guarantees physical soundness, while remaining fast and simple enough for routine laboratory use.

To address this gap we present Ophira, a reflectance-fitting tool that follows a data-first, physics-as-validation strategy. The refractive index is represented directly on a set of movable nodes, constrained only by general physical requirements (smoothness, monotonicity in the transparent region, optical-thickness anchoring) rather than by a chosen dielectric model, and KK consistency is imposed a posteriori, in rapid cycles, as a check on the retrieved dispersion rather than as a constraint built into the forward model. Because the adjusted parameters are the physical quantities themselves, the retrieval is both flexible enough to describe optically complex films and quick to adapt to structurally different samples, and it does not require choosing a mixing rule or committing to a microscopic picture of the porous medium. The refractive-index–thickness coupling in the fringe-bound optical thickness is resolved from spectra taken at several incidence angles through the Snell and Bragg relations, and a dedicated single-spectrum procedure (the *d*-scan) provides a robust thickness determination when only one near-normal-incidence spectrum is available. We validate the method on porous silicon over a range of porosities, including the high-porosity regime where EMA and oscillator models struggle, cross-check the retrieved thickness against scanning electron microscopy (SEM) measurements and against an established oscillator-based analysis, and discuss the reliability of n and d and the honest uncertainty attached to them. In this sense Ophira is not proposed as a replacement for model-based tools but as an additional, complementary instrument in the physicist's toolbox, suited in particular to complex and imperfect films.

Unlike the variational [53] and B-spline [54] approaches, which represent the dielectric function on a dense basis and enforce KK consistency by construction within an over-determined ellipsometric measurement, Ophira works from unpolarized reflectance alone. Its robustness derives from the specific combination of direct node-based retrieval of *n* and *k*, multi-angle thickness triangulation complemented by the near-normal *d*-scan, and KK consistency used as an independent a-posteriori validation rather than an imposed constraint. It is this combination, rather than the interpolation of *n* and *k* as such, that constitutes the novelty of the approach.

2. The Ophira software

2.1. Purpose and scope

Ophira is a software for the retrieval of the optical constants of a thin film from its measured reflectance. It takes as input one or more reflectance spectra, acquired at one or several angles of incidence, and

returns the $n(\lambda)$, $k(\lambda)$ and d, together with the simulated reflectance that reproduces the measurement. Four angles are used here, namely 8°, 20°, 40° and 60°. The 8° and 60° angles are at or close to the limits of the incidence-angle range provided by the Lambda 950 spectrometer, while 20° and 40° are intermediate. The 8° and 20° spectra are used to decouple n and d through the Snell and Bragg relations, since their near-normal incidence makes them essentially immune to the birefringence-induced variation of the refractive index. The 40° and 60° spectra, at oblique incidence, are instead where that angle-dependent variation becomes observable.

The availability of the code enables a user with different needs to adapt it to their own measurement geometry. While Ophira was developed for PSi, whose disordered and highly tunable structure makes it a demanding test case, nothing in its construction is specific to that material, so that it applies and can be easily adapted to other complex or imperfect thin films on an absorbing substrate. The program is built around a single guiding choice, that the quantities adjusted during the fit are the physical quantities themselves, the index and the thickness, rather than the parameters of an assumed dielectric model, and every functionality described below follows from that choice. A screenshot of the main window of the software is shown in Fig. 2.

2.2. The retrieval strategy

The strategy Ophira follows can be described as data-first and physics-as-validation. Rather than postulating a dielectric model, an effective-medium mixing rule or a set of oscillators, and then fitting its parameters, the program represents the dispersion of the film directly and constrains it only with requirements that any physical dielectric must satisfy, namely a smooth and monotonic behavior of the index in the transparent region and consistency with the KK relations. The KK consistency is not built into the forward model but is verified a posteriori, in rapid user-controlled cycles, and used as a diagnostic on the retrieved dispersion. This is what is meant by describing the approach as free of an assumed dielectric model while remaining physics-constrained, since the constraints applied are not a model of the material but general properties that its optical response is known to possess. The decreasing behavior of n and k away from the electronic resonances is an established experimental fact of normal dispersion, of a different epistemic standing from an effective-medium mixing rule, which imposes a particular way in which the microstructure combines the responses of its constituents. Imposing the former is therefore closer to enforcing a known behavior than to assuming a model, and it is what allows the same procedure to be used on films of very different porosities and microstructure without being reconfigured for each of them. A retrieval left entirely without such constraints would reproduce almost any spectrum and would carry no physical meaning, so the constraints are what make the result significant rather than what limits it. The practical consequence, developed in the Results section, is that a single workflow covers films from a few hundred nanometers to several micrometers in thickness and across a wide range of porosities.

2.3. Representation of the optical constants

The refractive index and the extinction coefficient are each represented on a set of 40 nodes distributed across the measured spectral range, whose values are the adjustable quantities of the fit. These are of two kinds, 14 nodes that the user controls directly and 26 further nodes that the fit places between them to keep the retrieved curve smooth, a division that was a deliberate design choice, made early in the development so that a reliable and smooth retrieval could be obtained without burdening the user with a large number of manual parameters, while the additional nodes still provide the resolution needed to follow the dispersion. In the range where the film is transparent or weakly absorbing, from about 420 nm up to the long-wavelength limit of the measurement at 2500 nm, the nodes of n are constrained to vary smoothly and monotonically, with a convex behavior consistent with normal dispersion, so that the retrieved index cannot develop the unphysical oscillations that an unconstrained point-by-point fit would allow. The monotonicity constraint can be switched off where the physics of the sample requires it, for instance when a material within the pores introduces its own dispersion feature, so that it acts as a default appropriate to the transparent region of a normally-dispersing film rather than as an unconditional rule. Below about 420 nm, where silicon absorbs strongly and the reflectance carries little information on the transparent-region dispersion, the corresponding nodes can be held fixed at the values obtained from the KK transform of the last free fit, which prevents them from fluctuating without physical justification, and a boundary node at 2550 nm is treated in the same way to anchor the long-wavelength end. Because k is small in the transparent region and is not the primary quantity of interest, it is determined together with n under the same constraints and, in the transparent region, it may be held at or near zero, a choice discussed in 2.6.

2.4. Interactive design and usability

Because the adjustable quantities are the optical constants themselves, the user interface acts directly on them: the index is adjusted through a set of sliders acting on the nodes, which makes the effect of every change immediately visible on the simulated spectrum, and the refractive index sliders can also be moved together so that the whole dispersion curve in the transparent region can be raised or lowered, or its slope changed, in a single action. This is a direct consequence of representing the index rather than a model of it, since the slider changes the optical response itself, whereas in a model-based fit one changes a parameter that acts on the response only indirectly, through the assumed dielectric function. The difference is most useful when the sample structure differs substantially from one measurement to the next, a situation in which a model-based description would have to be reconsidered each time, while here the same direct controls apply unchanged. A set of locking controls allows individual parameters to be held fixed during a fit, which is the standard approach used to avoid local minima and to explore the parameter space in a controlled way, without changing the physical constraints that the retrieval must satisfy, and a number of auxiliary tools for reading and inspecting the data, described in 2.7, support the retrieval at each step.

2.5. Thickness determination

Because n and d are coupled in the optical thickness that sets the position of the interference fringes, Ophira provides dedicated tools to determine d rather than leaving it as one fitting parameter among many. When spectra are available at more than one angle of incidence (Ophira considers 8°, 20°, 40° and 60°), d is obtained from the way the fringe positions shift with the angle moving from 8° to 20°, through the combination of the Snell and Bragg relations, which decouples the thickness from the dispersion. This procedure has been described in detail in the paper by G. Mula et al. [50].

When only a single near-normal-incidence spectrum is available, a procedure that we refer to as the d-scan is used, in which the user fits the same spectrum repeatedly for a series of assumed thicknesses and the way the retrieval responds to the assumed thickness is examined. This tool is designed to allow the user to explore four different windows where the evolution of several parameters is shown and compared across the whole range of fitting thickness d_{fit} values that the user explored. Several parameters are adjustable to let the user improve their experience. In a complex material as PSi, this tool is not to be intended as a strategy to mathematically determine an exact value for d, since in this kind of material there is no such a thing as the exact thickness for two main reasons. The first reason is that in a porous system the top surface can be rough, and the bottom porous/bulk interface has to be defined in

a region where the pore ends do not show a mathematically definable interface plane even in the best possible porous layer. The second reason stems from the homogeneity of the porous structure in the whole layer. Every gradient or fluctuation will act and modify the way the light sees the porous layer, so that the interference pattern will depend on the effective thickness seen by the light, d_{eff}, more than the absolute physical thickness d. The way the interface widens (the kind and shape of the gradient, for instance) will control what d_{eff} will be with respect to an SEM measured thickness d_{SEM}. Additionally, large-scale (in mm range) fluctuations in a thin film are invisible even to electron microscopy while being well within the range probed by the light beam in a tool as the Lambda 950. The d-scan tool, therefore, is aimed at guiding the user to the thickness range where the best possible d_{eff} is. A comment is fundamental here to separate the concepts: while the roughness mainly acts on the interference fringes amplitude and is controlled by a specific parameter slider in Ophira, the gradients will act in the vertical dimension of the porous layer, making the interface less defined. Even a sample with very flat SEM interfaces can show a compositional gradient that will affect the thickness value that is best adapted for the optimal fitting of the experimental data.

The principle of the d-scan tool is as follow: the user will compute a proper fitting of the reflectivity spectrum using a range of d_{fit} values that contains the effective thickness d_{eff}. This is a relatively easy task since for each reasonable d_{fit} is possible to find a companion value for n that satisfy the optical thickness determination from the fringes position. However, while the fitting can reproduce the fringes positions, there are a few signatures that will not be possible to simulate correctly. The d-scan is designed to allow the researcher to investigate the dependence on the thickness value used for the fitting, d_{fit}, of several parameters:

1. The simulated reflectivity R_{fit} vs the experimental reflectivity R_{exp};
2. The dispersion curve of the simulated refractive index n_{fit};
3. The total difference between R_{fit} and R_{exp} across the region where the porous layer absorption reduces the fringe contrast and the contrast evolution in the infrared (IR)
4. The reduced deviation of R_{fit} from R_{exp} in the whole spectrum and the sum of the KK residues.

The extraction and efficacy of these indicators is described in detail in the Results and discussion section.

2.6. Instrumental corrections

The reflectance measured on a real spectrometer departs from the ideal Fresnel-Airy response for reasons that are instrumental as well as physical, and Ophira includes a set of corrections that address them while preserving the information carried by the fringe positions. Lateral variations of the film thickness across the illuminated area average fringes of slightly different period and therefore damp the amplitude of the oscillations, and the program models this by fitting an inhomogeneity parameter that continuously adapts the calculated contrast to the measured one, so that the fit follows the real reduction of the fringe amplitude instead of forcing an agreement that the data do not support. A separate correction addresses the discontinuity that appears in the spectra of double-monochromator spectrometers such as the PerkinElmer Lambda 950 at the wavelength where the detector is changed, near 890 nm, which introduces a step and a change of the instrumental response in the IR. This correction can either be fitted or, through a dedicated function, measured directly from the data as the ratio of the mean reflectance levels on the two sides of the transition at 890 nm and then held fixed, which anchors it to the measurement and prevents the fit from absorbing the instrumental step into the retrieved index or absorption. A common feature of all these corrections is that they act on the amplitude of the fringes and never on their spectral position, so that the determination of the thickness, which rests on the fringe positions, is protected from them. The choice to hold the extinction coefficient at or near zero in the transparent IR belongs in the same context, since an unconstrained fit tends to introduce a small spurious absorption there in order to improve the amplitude agreement, and imposing k equal to zero removes this artefact at no cost to the quality of the reflectance fit.

2.7. Analysis and comparison tools

Beyond the fit itself, Ophira provides a set of tools to inspect and to validate the result. The positions of the reflectance maxima can be computed and displayed, which supports the thickness determination and gives an immediate check of the agreement between the measured and the simulated fringe pattern, and the retrieved index and absorption can be examined against their KK transforms as a measure of the internal consistency of the fit. The program can also load the results of an external fit and compare them, on the same measured spectrum and over the same spectral range, with its own, computing the reflectance residuals and the differences in the retrieved optical constants, which allows a direct and identical comparison between Ophira and a model-based tool. Results can be exported for further analysis and for the preparation of figures.

3. Methods

3.1. Forward model

The simulated reflectance $R(\lambda)$ is computed for a single homogeneous film on a semi-infinite substrate, using the standard Fresnel-Airy formalism for a stratified medium [60–62]. The substrate is treated as semi-infinite because the wafer backside is unpolished and scatters the transmitted IR out of the specular cone, so that no back reflection returns coherently.

Snell's law with complex indices gives the complex refraction angles, and the propagation cosine $\cos\theta_1$ in the film is evaluated on the physical branch, the one with non-negative real part, so that its real part sets the propagating component and its imaginary part the evanescent decay. At each interface ij the s- and p-polarized Fresnel amplitude reflection coefficients r_{ij}^{s} and r_{ij}^{p} are formed, with s the field perpendicular and p the field parallel to the plane of incidence. These expressions are standard and are collected in Appendices A and B.

3.1.1. Airy summation

Summing the multiple internal reflections in the film as a geometric series gives, for each polarization $\nu \in \{s,p\}$,

$$r^{\nu} = \frac{r_{01}^{\nu} + r_{12}^{\nu}\, e^{2i\varphi}}{1 + r_{01}^{\nu}\, r_{12}^{\nu}\, e^{2i\varphi}}, \qquad \varphi = \frac{2\pi}{\lambda} N_f\, d \cos\theta_1,$$

where r_{01}^{ν} and r_{12}^{ν} are the air-film and film-substrate Fresnel coefficients (see Appendix B) and φ is the phase accumulated in one traversal of the film. The one property of this formalism that the rest of the Methods relies on is that the fringe positions are set by the phase φ, and through it by the product $N_f\, d$. This underlies both the amplitude/position separation of the corrections and the thickness determination, and it is why the Airy relation is kept here in full.

3.1.2. Unpolarized combination

The Lambda 950 source provides no controlled polarization, so the polarization degrees of freedom are not identifiable from the data. The film is therefore treated as isotropic and the modelled reflectance is the equal-weight average of the two polarizations,

$$R(\lambda) = 1 \Big/ 2\Big(|r^{s}|^2 + |r^{p}|^2 \Big) \cdot 100,$$

the factor 100 expressing R in reflectance percent to match the measured

spectra, a scaling carried consistently through the correction terms below. Leaving the polarization weight, the uniaxial birefringence and the s/p coherence phase free would let the fit assert what the data cannot constrain, so these are fixed (weight 0.5, birefringence and coherence phase zero) and the residual, unquantifiable contrast losses are moved into a single explicit envelope term, described below.

3.2. Amplitude corrections

The Fresnel-Airy model departs from the measured spectra for instrumental and physical reasons: surface roughness, volume scattering, lateral thickness inhomogeneity across the illuminated area, and the detector-change discontinuity of the spectrometer. Ophira applies a set of corrections for these effects that share one property, they act only on the amplitude of the interference fringes and never on their spectral position. Because the thickness is carried by the fringe positions, this amplitude/position separation protects the thickness determination from every correction below.

3.2.1. Roughness and volume scattering

A Debye-Waller-type factor damps the internally propagating field,

$$f_{\mathrm{scatt}}(\lambda,\theta_1)=\exp\left[-\frac{\mathrm{scatt}}{130}\left(\frac{500}{\lambda}\right)^{1.6}\frac{1}{\cos\theta_1}\right],$$

where scatt is a single fitted amplitude (dimensionless), λ is in nanometres and the constants 130 and 500 nm are empirical scale factors. The division by $\cos\theta_1$ accounts for the longer optical path at oblique incidence, and at normal incidence the factor reduces to $\exp\left[-(\mathrm{scatt}/130)(500/\lambda)^{1.6}\right]$.

3.2.2. Lateral inhomogeneity

Thickness variations across the illuminated area average fringes of slightly different period and damp the oscillation amplitude. Defining the thickness spread $\sigma_d = d\,(\mathrm{inhom}/100)$, in which inhom is the fitted fractional thickness spread as a percentage, two phase terms are formed, a normal-incidence contribution ϕ_{norm} and a geometric contribution ϕ_{foot} that appears at oblique incidence,

$$\phi_{\mathrm{norm}}=\frac{\pi\, n_f\,\sigma_d\cos\theta_1}{\lambda},\qquad \phi_{\mathrm{foot}}=\frac{\pi\, n_f\,\sigma_d\,(1/\cos\theta_0-1)}{\lambda},$$

and the damping factor is

$$f_{\mathrm{amp}}=\exp\left[-2\left(\phi_{\mathrm{norm}}^2+\phi_{\mathrm{foot}}^2\right)\right].$$

At normal incidence ϕ_{foot} vanishes, while near 60° it becomes comparable to ϕ_{norm} (since $1/\cos 60^\circ - 1 = 1$). This factor multiplies only the oscillating part of the reflectance, leaving the fringe-free mean unchanged.

3.2.3. Contrast envelope

Residual, unquantifiable losses of fringe visibility (imperfect source polarization, wavelength-dependent goniometer optics, partial coherence) are lumped into a smooth envelope $V(\lambda)$ that scales only the oscillating part of the spectrum and leaves the fringe-free mean unchanged,

$$R_{\mathrm{coh},d}(\lambda)=R_{\mathrm{mean}}(\lambda)+V(\lambda)\,[R_{\mathrm{coh}}(\lambda)-R_{\mathrm{mean}}(\lambda)]\,f_{\mathrm{amp}},$$

$$R_{\mathrm{mean}}=1\Big/2\left(|r_{01}^{s}|^2+|r_{01}^{p}|^2\right)\cdot 100,$$

where R_{coh} is the full coherent reflectance of the Airy summation and R_{mean} is the interface-only reflectance obtained by setting the film-substrate coefficient $r_{12}^{\nu}\to 0$, so that $V(\lambda)$ scales the fringe modulation about the fringe-free mean. The envelope is a vertex-form parabola with a directly controllable vertex wavelength λ_v,

$$V(\lambda)=f_{c0}+f_{cc}\left(\frac{\lambda-\lambda_v}{1000}\right)^2,\qquad \lambda_v=1500+1000\,f_{cv},$$

clipped to $[0,3]$, in which f_{c0} is the overall level, $f_{cv}\in[-2,2]$ sets the vertex wavelength and f_{cc} the curvature. Placing the vertex outside the measured band makes V monotonic across the band, and $f_{cc}=0$ gives a constant $V=f_{c0}$, which is the default.

3.2.4. Global Debye-Waller term

A further Debye-Waller factor is applied to the whole reflectance, not only to its oscillating part, to reproduce the damping of the silicon substrate features,

$$f_{\mathrm{DW}}=\exp\left[-0.013\,\frac{\mathrm{scatt}}{130}\left(\frac{500}{\lambda}\right)^2\frac{1}{\max(\cos^2\theta_0,\,0.1)}\right],$$

with the constant 0.013 calibrated empirically. Its typical effect is below 2% at 8°, rising to about 15% at 60° in the ultraviolet for large scattering (scatt ≈ 100).

3.2.5. Detector-change correction

The Lambda 950 switches detector (photomultiplier to PbS) at $\lambda =$ 890 nm, which introduces a multiplicative step and a non-flat instrumental response in the IR. For $\lambda > 890$ nm Ophira applies

$$R(\lambda)\to R(\lambda)\,k_j\left(\frac{890}{\lambda}\right)^{\alpha}\exp\left[-\beta\,\frac{\lambda-890}{1000}\right],$$

in which k_j is a multiplicative jump, α a spectral-curvature exponent and β an exponential damping, each capturing a distinct feature of the transition. The same factor is used in the forward model, as a multiplication, and in the maxima extraction, as a division, so that the correction cannot displace the peak markers. Alternatively, the jump can be measured directly from the data of a given angle as the ratio of the mean reflectance levels just above and just below the transition,

$$k_{j,\mathrm{meas}}=\frac{\overline{R}_{\lambda>890}}{\overline{R}_{\lambda<890}},$$

and then locked, which anchors it to the measurement and prevents the fit from absorbing the instrumental step into n, k or the scattering; the measured jump varies with sample and angle, typically decreasing from 8° to 60°.

3.2.6. Assembly and additive offset

The corrections are applied in a fixed order. The scattering factor damps the internal propagation, the inhomogeneity factor and the contrast envelope act on the oscillating part to give $R_{\mathrm{coh},d}$, the global Debye-Waller factor multiplies the whole reflectance, and a constant additive offset offs (default 1%) compensating residual dark current and baseline is added last,

$$R(\lambda)=R_{\mathrm{coh},d}(\lambda)\,f_{\mathrm{DW}}(\lambda)+\mathrm{offs}.$$

3.3. Representation of the optical constants

Ophira design $n(\lambda)$ and $k(\lambda)$ dispersion curves using a set of 40 nodes across the measured range, whose values are the free parameters of the fit, and the continuous curves are obtained by piecewise cubic Hermite interpolation (PCHIP) of the nodes onto the spectral grid, chosen over a cubic spline because it is monotonicity-preserving and does not introduce the overshoot between nodes that a spline would allow. The 40 nodes are of two kinds: 14 user-controllable nodes, which the operator adjusts directly, and 26 additional nodes, which the fit places between them so that the retrieved curve stays smooth without requiring manual control of every point. Keeping the number of hand-controlled nodes

small is a deliberate design choice, made so that a reliable and smooth retrieval can be obtained without burdening the user with a large number of manual parameters, while the additional nodes carry the resolution needed to follow the dispersion. In the transparent and weakly absorbing range, from about 420 nm to the long-wavelength limit of the measurement, the nodes of n are constrained to vary smoothly and monotonically with a convex shape consistent with normal dispersion. The monotonicity constraint is a default appropriate to this range and can be switched off where the physics of the sample requires it. Below about 420 nm, where silicon absorbs strongly and the reflectance carries little information on the transparent-region dispersion, the corresponding nodes are held fixed at the values given by the KK transform of the last free fit, and a boundary node at the long-wavelength end is treated in the same way.

3.4. Kramers-Kronig consistency

KK consistency is used not as a passive check applied once at the end, but as an iterative constraint folded back into the retrieval until the fitted index and the index implied by the fitted absorption agree. At each step the code computes $n_{\mathrm{KK}}(\lambda)$ from the current $k(\lambda)$ through a multiply-subtractive KK relation with one subtraction (MSKK-1), written for the real part of the dielectric function $\varepsilon_1(E)$ as

$$\varepsilon_1(E) - \varepsilon_1(E_{\mathrm{IR}}) = \frac{2}{\pi}\left(E^2 - E_{\mathrm{IR}}^2\right) \mathscr{P} \int_0^{\infty} \frac{E'\,\varepsilon_2(E')}{\left(E'^2 - E^2\right)\left(E'^2 - E_{\mathrm{IR}}^2\right)}\, dE',$$

where E is the photon energy, E' the integration variable, $\varepsilon_2 = 2nk$, the imaginary part of the dielectric function, evaluated from the current n and k, $\mathscr{P}$ the Cauchy principal value, and $E_{\mathrm{IR}} = 1240/2500$ eV an IR anchor at 2500 nm, a wavelength at which PSi is transparent and n is well known. Subtracting the constant $\varepsilon_1(E_{\mathrm{IR}})$ cancels the unknown contribution of the high-energy states outside the computation range and makes the result relative to a measurable anchor. The principal value is regularized with a punctum excisum, excluding grid points within $|E' - E| < 2.5\,\Delta E$ of the evaluation energy E (with ΔE the grid spacing), and the transform is evaluated on an equispaced energy grid (35000 points between 0.05 eV and 30 eV) and lightly smoothed with a Savitzky-Golay filter of polynomial order 3.

The agreement between the fitted and the transformed index is quantified by the root-mean-square difference

$$\mathrm{RMS}(n - n_{\mathrm{KK}}) = \sqrt{\frac{1}{N}\sum_{i=1}^{N}\left[n(\lambda_i) - n_{\mathrm{KK}}(\lambda_i)\right]^2},$$

evaluated over the free nodes above 420 nm, with N the number of such nodes. Alongside $\mathrm{RMS}(n - n_{KK})$, the local scatter of the transformed index is quantified by σ_{local}, the standard deviation of the raw n_{KK} evaluated in a short sliding window (15 grid points) and averaged over the free nodes above 420 nm; it measures the intrinsic noise of the KK computation, independent of any smoothing. The consistency is then summarized by the ratio $\mathrm{RMS}/\sigma = \mathrm{RMS}(n - n_{KK})/\sigma_{local}$, which compares the systematic fit-to-transform deviation with this local noise. Because it is referred to each retrieval's own noise level, RMS/σ is comparable across samples of different quality: a value of order or below three indicates a deviation at the noise level, hence a consistent retrieval, whereas a markedly larger value signals a significant inconsistency, most often a wrong thickness. This quantity guides an iterative use of the transform.

A typical strategy is the following. The user fits the reflectance and evaluates the metric; where the agreement is poor, the transformed values n_{KK} can be pushed into the index nodes $n(\lambda)$ and the spectrum refitted from that starting point, the operation being repeated until index and absorption are mutually consistent. The software provides the transform, the injection and the metric as tools; it does not prescribe a fixed number of cycles or an automatic acceptance criterion, because a complex retrieval on an unknown material cannot be reduced to a closed recipe and the user retains judgement over how far to push each step, as with any fitting tool for materials whose dielectric response is not known in advance. What the physics does impose is a boundary condition on the thickness: because d controls the fringe positions, the cycle can only be brought to consistency for a sound estimate of d, since at a wrong thickness no index is simultaneously reflectance-consistent and KK-consistent, so a persistent failure to reach consistency points to the thickness rather than to the index.

When the index fit remains unstable, that is $n(\lambda)$ keeps departing strongly from $n_{\mathrm{KK}}(\lambda)$ even at a reasonable d, the consistency can instead be routed into the absorption. Locking the index nodes and running a fitting session with n and d held leaves only $k(\lambda)$ free to match the reflectance, which moves the injected KK-consistent index into a matching absorption; releasing the index nodes and fitting once more then normally recovers consistency. In all cases the residual freedom lies in the strongly absorbing region, where the reflectance carries little information on the transparent-region dispersion and the retrieval has correspondingly little control, and where the KK transform, evaluated over a finite spectral range, is mathematically weakest at the ends of that range, so the largest node-to-node discrepancies are expected there rather than in the transparent interior. The truncation of the integral at the low-energy end introduces such a boundary artefact at the longest-wavelength node, which is handled by locking that node during the cycles when it drifts.

3.5. Fit objective and optimization

The retrieval minimizes a functional that combines the data residuals with physical and numerical constraint terms,

$$\chi^2_{\mathrm{tot}} = \sum_i w(\lambda_i)\left[R(\lambda_i) - R_{\mathrm{exp}}(\lambda_i)\right]^2 + \chi^2_{\mathrm{constraints}}.$$

For the near-normal configurations (8° and 20°) the spectral weighting is uniform, $w(\lambda) = 1$. For the oblique configurations (40° and 60°) a non-uniform weighting emphasizes the region where the fringes are well modulated and the instrumental parameters separate identifiably,

$$w(\lambda) = \begin{cases} 0 & \lambda < \lambda_{\min} \\ 15 & 400 \le \lambda < 600 \\ 40 & 600 \le \lambda \le 1300 \\ 0.5 & \lambda > 1500 \\ 1 & \text{otherwise} \end{cases} \qquad (\lambda \text{ in nm})$$

with an additional penalty $40\sum_i \left(R - R_{\mathrm{exp}}\right)^2$ for $\lambda < \min(500, \lambda_{\min})$ that replaces the missing transparency data in the ultraviolet, and $\lambda_{\min}$ (default 450 nm) the threshold below which the data are not considered reliable. For the oblique fits a strong anchoring term penalizes departures of the mean optical thickness $\langle n\rangle d$ from the value $\langle n\rangle_0 d_0$ fixed at the start of the fit,

$$\chi^2_{\langle n\rangle d} = W\left(\frac{\langle n\rangle\, d - \langle n\rangle_0\, d_0}{\langle n\rangle_0\, d_0}\right)^2, \qquad W \approx 10^9,$$

where $\langle n\rangle$ is the mean refractive index over the transparent range and W a large penalty weight, active only beyond a 1% dead zone. This term blocks the $n{\cdot}d$ degeneracy, which is inherent to fringe-position information at a single angle because moving n and d jointly in inverse proportion leaves the fringe positions unchanged, and it holds the oblique fit close to the near-normal solution that has already resolved the degeneracy geometrically.

Table 1
Thickness values obtained at four incidence angles for a SiO_2 layer on Si with nominal thickness of 300 nm using Ophira and a literature fixed-values dispersion curves for $\boldsymbol{n}$ and $\boldsymbol{d}$.

Angle (deg)	d (nm)	Deviation from nominal (%)
8	298.7	-0.42
20	298.7	-0.42
40	302.9	+0.98
60	307.8	+2.60

3.6. Thickness determination

3.6.1. Multi-angle triangulation

A reflectance maximum of order m occurs when the double-pass phase is a multiple of 2π,

$$2\,n_f\,d\cos\theta_1 = m\,\lambda, \qquad \cos\theta_1 = \sqrt{1-\sin^2\theta_0\big/n_f^2}.$$

Observing the same order m at two nearby angles θ_A and θ_B, at wavelengths λ_A and λ_B where the dispersion of $n_f(\lambda)$, that is the real part of the complex refractive index N_f, is essentially equal, eliminates n_f between the two Bragg conditions and yields it from geometry alone,

$$n_f = \sqrt{\frac{\sin^2\theta_A - (\lambda_A/\lambda_B)^2\sin^2\theta_B}{1-(\lambda_A/\lambda_B)^2}},$$

after which the thickness follows by substitution into the Bragg condition,

$$d = \frac{m\,\lambda_A}{2\,n_f\cos\theta_{1,A}}.$$

This determination uses only the measured maxima positions and assumes no functional form for $n(\lambda)$, so it is model-independent. It is implemented for the 8°/20° pair.

In practice this determination is automated. Starting from a reasonable fit at 8°, the procedure transfers that solution to 20° and fits there, then estimates the thickness d from the way the fringe maxima shift between the two near-normal angles, through the combined Snell and Bragg relations. Rather than imposing this estimate directly, the fit thickness d_{fit} is migrated towards the estimated d in small steps, with the refractive-index nodes re-adjusted at each step while d_{fit} is held fixed, so that $n(\lambda)$ and $k(\lambda)$ remain mutually consistent as d_{fit} evolves and the fit quality is preserved. Once the thickness has converged, all available angles are fitted simultaneously, with the oblique-incidence spectra held close to the near-normal solution that has already resolved the degeneracy geometrically. These two steps correspond to the FIT AUTO and FIT MULTI procedures of the program, described in detail in the manuals.

3.6.2. Single-spectrum d-scan

When only one near-normal spectrum is available the thickness is determined by scanning it. The same spectrum is fitted for a series of assumed thicknesses d_{fit}, and the response of the retrieval to the assumed value is examined through two independent observables that the physics of the film makes sensitive to an incorrect thickness.

Reflectance-fringe test. In the range where fringes are present, their positions obey the Bragg condition $2n_f d\cos\theta_1 = m\lambda$, so they are set by the product $n_f d$. Along a fringe of fixed order this product is fixed, hence a change of the assumed thickness must be compensated by an opposite change of the retrieved index,

$$\frac{\delta d}{d} \approx -\frac{\delta n_f}{n_f} \qquad \text{(fixed order)}.$$

A single wrong thickness cannot, however, reproduce the whole fringe pattern: the compensation that fixes one order misplaces the others, because the orders scale differently with wavelength, so an incorrect thickness leaves a reflectance mismatch that no smooth adjustment of $n(\lambda)$ can remove. The mismatch between the simulated and the measured fringe pattern is therefore an indicator that the assumed thickness is wrong.

Index-continuity test. In the strongly absorbing region, the reflectance carries no fringe information on the optical thickness, so the index retrieved there is fixed by the KK extrapolation and is essentially independent of the assumed thickness. In the fringe region the index does depend on it, through the compensation above. At the correct thickness the fringe-region index joins continuously onto the thickness-independent value of the absorbing region; at an incorrect thickness the two do not match and a step Δn appears at the boundary between the two regions, in the same spectral interval where the reflectance mismatch is largest. The sign of the step is diagnostic: an underestimated thickness forces an overestimated index and a step upward, an overestimated thickness forces a step downward. This is the most reliable indicator, since it does not depend on users' fitting skills and on fringes amplitude but just on the maxima positions.

The two observables respond to the same error through different quantities, the reflectance through the fringe positions and the index through its continuity across the transparent-to-absorbing boundary, and together they identify the range of thicknesses over which the retrieval is consistent. In a material with fuzzy, that is spatially extended, interfaces a single exact thickness is not a meaningful target, and the relevant quantity is the effective thickness that describes the optical behavior of the sample; the honest output of the procedure accordingly is an interval whose width is the associated uncertainty. This width is sample-dependent, from a few nanometres on the trivial calibration case up to several tens of nanometres on the complex porous

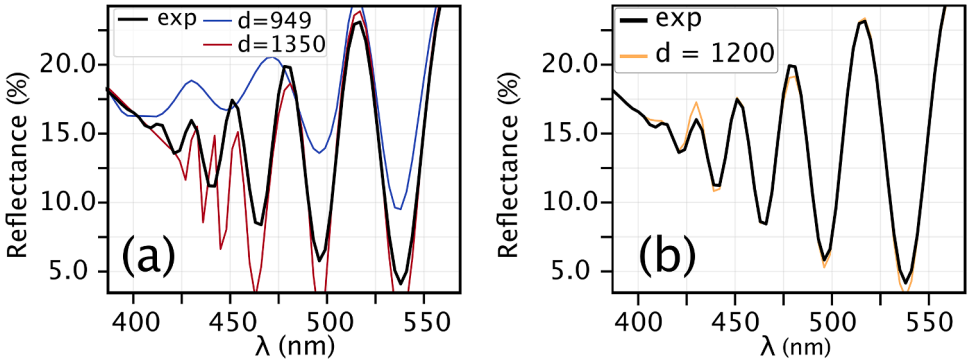


Fig. 3. Behavior of the $\boldsymbol{R_{fit}}$ vs $\boldsymbol{R_{exp}}$ for several values of $\boldsymbol{d_{fit}}$. In (a) $\boldsymbol{R_{exp}}$ is compared with the best fitting obtained using a larger and a smaller value of $\boldsymbol{d_{fit}}$ with respect to $\boldsymbol{d_{eff}}$. In (b) $\boldsymbol{R_{exp}}$ is compared with a fit obtained using the correct value of $\boldsymbol{d_{fit}} \approx \boldsymbol{d_{eff}}$. The best $\boldsymbol{d_{eff}}$ is $\boldsymbol{d_{eff}} \approx 1200$ nm. The plots are direct output of Ophira within the $\boldsymbol{d}$-scan analysis.

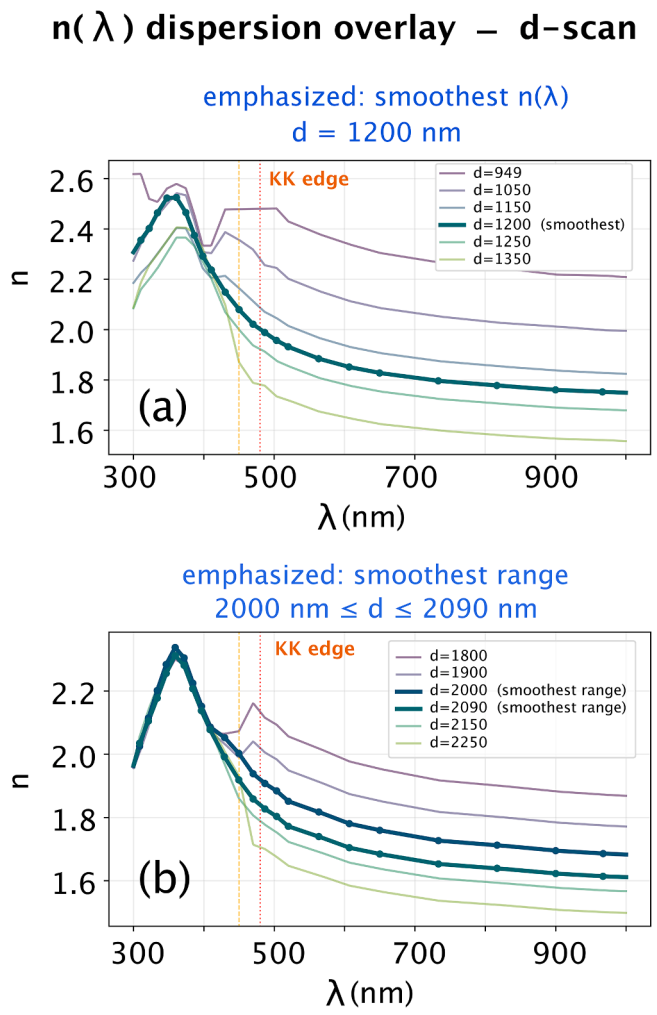


Fig. 4. Evolution of the fitted ***n*** dispersion curves as a function of d_{fit}. (a) The panel refers to the same sample of Fig. 3 and the plot also in this case suggests that the best d_{eff} is $d_{eff} \approx 1200$ nm. (b) Example of the same plot for another sample, where more than one curve has been emphasized. This put into clear evidence a thickness range compatible with a regular ***n*** dispersion curve. The plot is a direct output of Ophira within the ***d***-scan analysis.

layers, and is bounded below by the few-tens-of-nanometres floor below which an optical thickness of PSi cannot be determined.

Additional *d*-scan windows. The *d*-scan also presents the user two additional windows reporting the superposition of the simulated and experimental reflectivity spectra and the evolution of the residuals in reflectivity and KK residuals for a more complete evaluation. Several adjustments in the considered spectral regions are available. While the index continuity test is the most reliable, the other indicators are also useful and for optimal fittings in regular samples all converge to the same d_{eff} values range.

The novelty lies in the specific combination of a flexible, node-based representation of $n(\lambda)$ and $k(\lambda)$ with physically motivated bounds (monotonicity, convexity, normal dispersion and KK consistency). Because the representation is flexible yet physically constrained, the continuity and regularity of the retrieved $n(\lambda)$ become a sensitive and physically meaningful criterion for the effective thickness: the correct d_{eff} is the one for which a regular, physically admissible dispersion reproduces the reflectance. To our knowledge, using the regularity of a constrained but non-parametric $n(\lambda)$ as the primary discriminant for d_{eff} in reflectance-only retrieval has not been formulated in this way, and it distinguishes Ophira from both fixed-dispersion model fitting and from unconstrained point-by-point or B-spline optical-constant extraction.

3.7. Uncertainty estimation

For each node the uncertainty is estimated from the local curvature of the residual sum of squares S, obtained by perturbing that single node by $\pm\varepsilon$ (with $\varepsilon = 10^{-4}$) and forming the second difference,

$$H_{jj} = \frac{S(x_j+\varepsilon) - 2S(x_j) + S(x_j-\varepsilon)}{\varepsilon^2}, \qquad \sigma_j \propto \frac{1}{\sqrt{H_{jj}}}.$$

The estimate is indicative rather than rigorous: it uses only the diagonal of the Hessian and neglects the parameter covariances, and its scale is taken from the residual sum of squares itself, which is circular for a proper variance-based error estimate and does not incorporate a separate instrumental-noise. It is reported as an indication of the relative node-to-node confidence, not as a rigorous confidence interval, a point returned to in the discussion of reliability.

3.8. Deviation metric

Throughout this work the quality of a reflectance fit is quantified by the root-mean-square deviation between the simulated and the measured reflectance, in reflectance percent,

$$\mathrm{RMSE}(\%R) = \sqrt{\frac{1}{N}\sum_{i=1}^{N}\left[R(\lambda_i) - R_{\mathrm{exp}}(\lambda_i)\right]^2}.$$

This is the square root of the mean of the squared data residuals and involves no normalization by an assumed measurement variance, so it is a plain data-residual metric and not a reduced χ^2. It is a measure of fit fidelity to the data and is not, by itself, a measure of the physical correctness of the retrieved constants, a distinction developed in the Results and Discussion.

3.9. Software development and use of AI-assisted tools

The Ophira software was developed with the assistance of generative AI coding tools. The initial code base was generated with Google Gemini 3.1 and was subsequently developed and refined with Anthropic Claude (Sonnet 4.6, Opus 4.7 and Opus 4.8). All programming was carried out through these tools; the author is not a professional programmer. The physical model, the fitting strategy, the constraints, the validation and every scientific conclusion reported here are the author's own: the author specified the physics and the algorithms to be implemented, tested the resulting behavior against experimental data, and critically reviewed, corrected and accepted or rejected the tools' output at each step. The AI tools were used as an implementation instrument under continuous human oversight, and the author takes full responsibility for the content of the software and of this work. The tools were not used to design the experiments, to interpret the measurements or to draw the conclusions. Code development and scientific review were deliberately kept in separate working sessions, one used to write and revise the code and a separate one used to examine the physics, the validation and the manuscript, so that the scientific assessment was carried out independently of the code generation. Beyond the two-session separation of code writing and scientific review, individual code implementation choices and critical code segments were frequently cross-checked against independent AI sessions using different models, so that no single generation was accepted without an independent implementation being consulted.

This development model shows that a domain scientist can efficiently direct AI-assisted tools to implement a physically grounded analysis tool while retaining full scientific control over the method and its validation.

4. Results and discussion

To describe the capability of Ophira, a first test of general validity

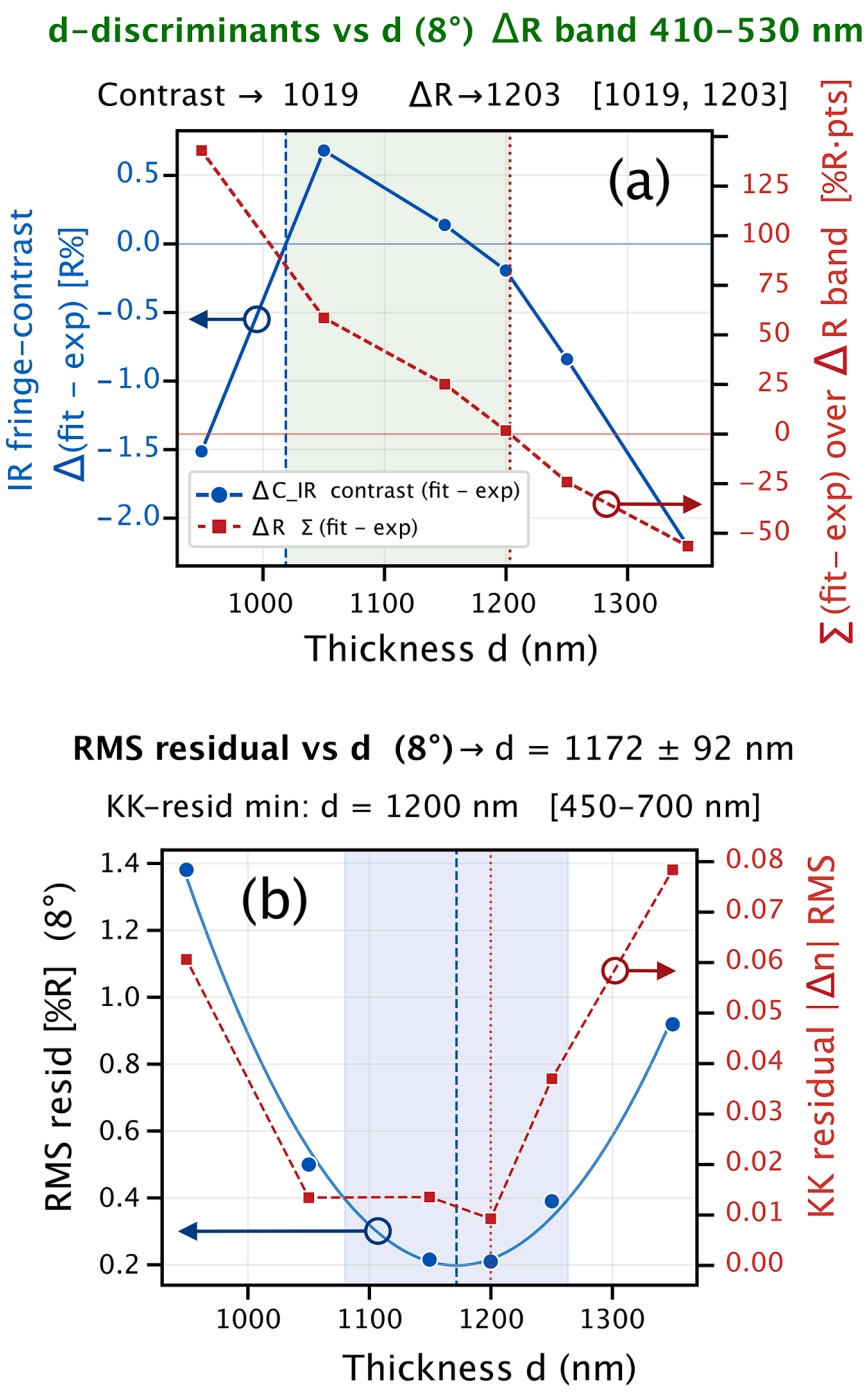


Fig. 5. Third and fourth panels of ***d***-scan. (a) Evolution of the distance between R_{fit} and R_{exp} for the spectral region described in Fig. 3. The best d_{eff} is $d_{eff} \approx 1200$ nm as in Fig. 3 and Fig. 4(a). A weaker indicator is the evolution of the fringe contrast in the IR range (in this case 890 – 2500 nm). Please note that also this indicator has one of the 0-crossing close to 1200 nm. (b) Deviation and KK residues as a function of d_{fit}. The best d_{eff} is again $d_{eff} \approx 1200$ nm as in Fig. 3 and Fig. 4(a) demonstrating the coherence of the four panels. The plots are a direct output of Ophira within the ***d***-scan analysis. The solid blue curve in panel (b) is a parabolic fit to the RMS residuals, used to locate the most probable position of the minimum (and hence the effective thickness); it is not an eye guide.

has been performed on an easy material, that is by fitting a commercial sample consisting on commercial (300 ± 15) nm wet thermal SiO_2 film on a highly boron-doped Si from Siegert Wafer. In this case there is no uncertainty on all parameters, since the optical properties are tabulated and the roughness is negligible.

4.1. *SiO_2-on-Si validation (calibration test)*

The nominal oxide thickness indicated by the seller (3000 Å ±5%, wet thermal oxide) gives an acceptance window of [285, 315] nm. The refractive index $n(\lambda)$ is fixed to the literature dispersion of thermal SiO_2

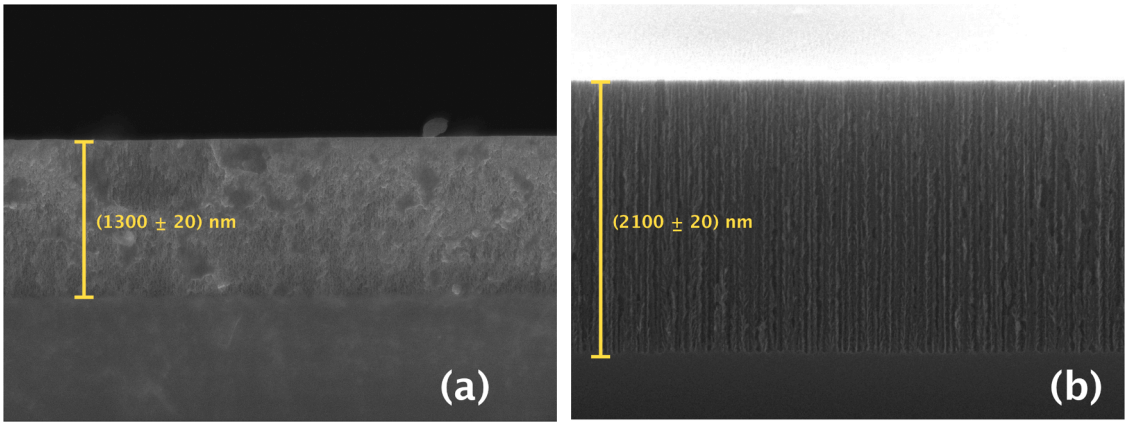


Fig. 6. SEM cross section of the medium(a) and high (b) porosity samples described in § 4.2.2.

($\sigma_n = 0$), $k = 0$, so that the only geometric free parameter is the thickness d. The only real parameter is the thickness d and, in this case $d_{SEM} = d_{eff}$ because the material is homogeneous and the interfaces are atomically flat. This is a proofing test on a well-characterized commercial sample: it certifies that the fit engine returns the correct thickness on a known material at every incidence angle.

The results shown in Table 1 clearly show that all four thicknesses fall well inside the ±15 nm nominal window. In particular, the worst-case deviation is +7.8 nm at 60°, against a ±15 nm tolerance. The near-normal angles (8°, 20°) return identical $d = 298.7$ nm, agreeing with the nominal 300 nm to within 0.5%. These are the angles used to decouple n and d, and the calibration confirms they do so accurately on a known material. The contrast corrections (scatt, inhom) were zero at all four angles, so on this smooth, homogeneous oxide only the IR correction and the additive offset act. This is the expected behaviour for a well-behaved calibration sample and is consistent with the corrections acting on the fringe amplitude, not on the fringe position that sets the thickness.

4.2. Thickness determination

The first step for a correct simulation of R_{exp} is the use of the correct thickness. An important reminder here is that, as discussed in section 2.5, even having an SEM cross section image does not guarantee that the SEM-determined physical value is necessarily the best possible value for the correct identification of the thickness value that best represent the thickness seen by the light beam. We'll refer to this value as the effective thickness d_{eff}. The best fittings will be obtained when $d_{fit} = d_{eff}$. The d-scan method, described in § 3.6.2, is built to efficiently and reliably help the experimenter to identify a reasonable range for d_{eff} and therefore obtain optimized fitting, representing therefore a very useful Ophira's tool.

4.2.1. d-scan tool

The d-scan method is composed of four different panels that highlight different aspects of the behavior of different parameters as d_{fit} is varied. In this paragraph we are going into further details on how the method works and show the reliability of those indicators in the determination of the d_{eff} value.

The first panel is the reflectance itself: in the spectral region where the interference fringes contrast is progressively reduced because of the absorption, the correct simulation R_{sim} of the experimental spectrum R_{exp} depends more on d than on n. Therefore, the simulated spectra in that region will go from above to below R_{exp} by varying d_{fit}. This is shown in Fig. 3, where the best fits for different values of d_{fit} are shown. In (a) it is shown that two pieces of information are extracted from the plot: the absolute value of R_{fit} does not match R_{exp}, being lower that R_{exp} for $d_{fit} > d_{eff}$ and vice versa for $d_{fit} < d_{eff}$. At the same time, the fit fails to correctly follow the fringe pattern. In (b) the correct value of d_{eff} is used, and both the absolute R value and the fringe positions are matched. This demonstrates how the mismatch between the simulated and the measured reflectance is a direct and reliable indicator when the assumed thickness is wrong.

The second d-scan panel is the continuity of the retrieved index across the boundary between the transparent and the absorbing regions: where the film absorbs strongly the reflectance carries no fringe information on the optical thickness, so the retrieved index there is fixed by the KK extrapolation and is essentially independent of the assumed thickness, whereas in the fringe region the index does depend on it, an underestimated thickness being compensated by an overestimated index and conversely. When d_{fit} matches d_{eff} index retrieved in the fringe region joins smoothly onto the thickness-independent value of the absorbing region, while at an incorrect d_{fit} the two do not match and a step appears at the boundary, upward for an underestimated thickness and downward for an overestimated one, in the same spectral region where the reflectance mismatch is largest. The d-scan detects the regularity and points to the user the curves that most match the Cauchy regularity criterion (see Methods for details). This is shown on Fig. 4(a) for the same sample of Fig. 3.

An important note about the uncertainty of the d_{eff} value. When the d-scan detects more than one n dispersion curve that satisfy the regularity range, then it indicates two curves and, if needed, a range. This is evidenced in Fig. 4(b) for another sample.

The third d-scan panel shows the evolution of the fitted vs experimental curves reflectivity difference in the region where the absorption rapidly increases, blue curve Fig. 5(a), and the evolution of the difference in the contrast of the interference fringes in the IR region for the fitted and experimental reflectivity spectra, red curve in Fig. 5(a). These indicators are most useful when the measured spectra are regular.

The fourth d-scan panel shows the last two indicators: the deviation of R_{fit} with respect to R_{exp} and the KK residues. For optimized fits the two indicate the same d_{eff} range, while they may flutter if the fits are not optimized. These parameters are shown in Fig. 5(b) and suggest the same d_{eff} than the other indicators. Please note that these two indicators are sensitive to the quality of the experimental spectra and the quality of the fittings made by the user, since the shape of the fitted reflectivity spectra and the simulated n dispersion curves are tightly related to how accurately those fittings were performed.

All indicators therefore point to the same conclusion from different observables, and together they identify the range of d_{eff} over which the retrieval is consistent rather than a single value. The mathematical procedures for the extraction of these data are given in the Methods.

Please note that the value of d_{eff} is necessarily defined within a range that, while difficult to estimate in a general rule since the uncertainty

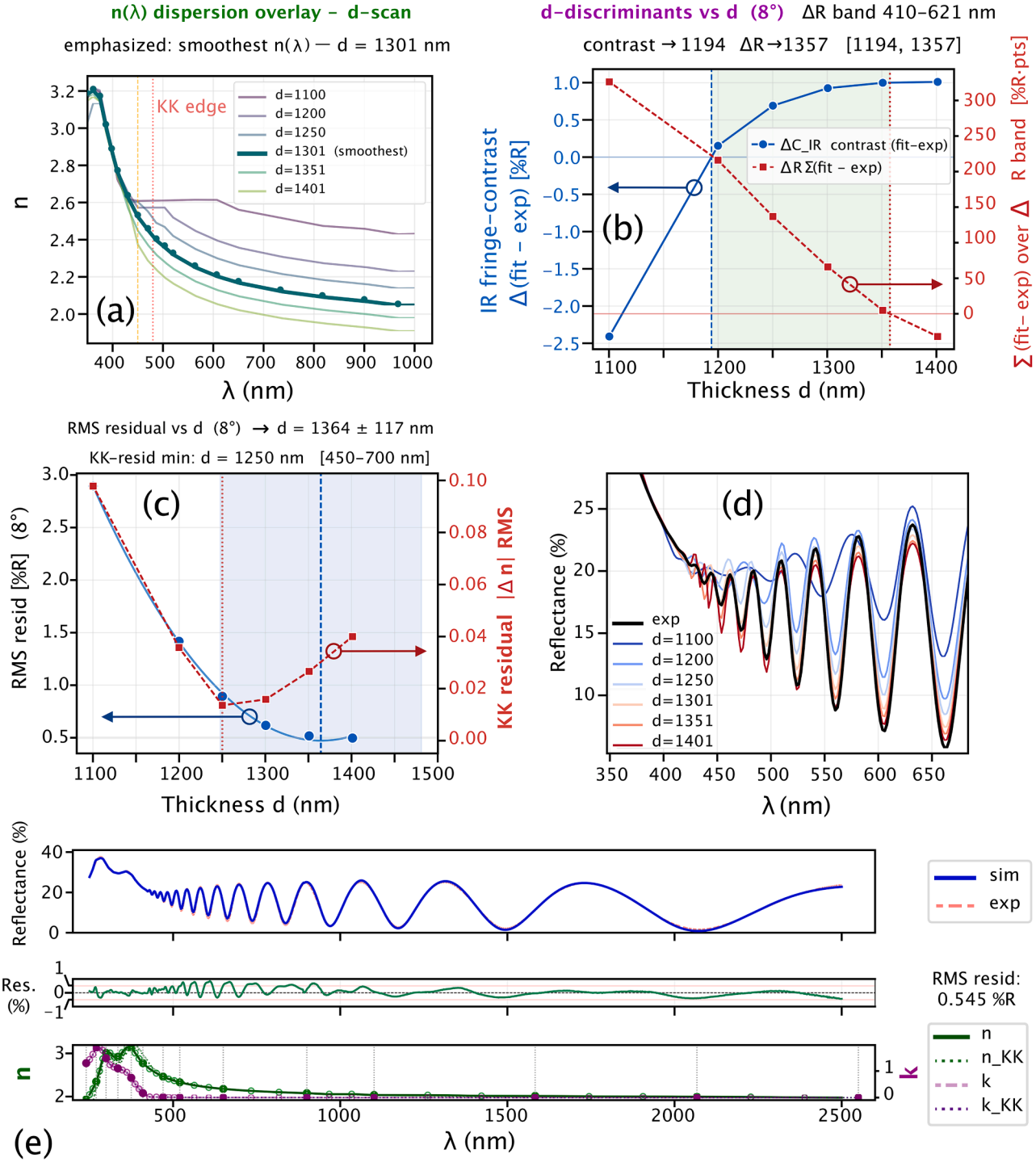


Fig. 7. ***d***-scan analysis, (a) through (d), for the sample in Fig. 6(a). The fitting results obtained using the optimal d_{fit} are also shown, (e). The solid blue curve in panel (c) is a parabolic fit to the RMS residuals, used to locate the most probable position of the minimum (and hence the effective thickness); it is not an eye guide. Magnified panels in full resolution are available in the supplementary material S1.

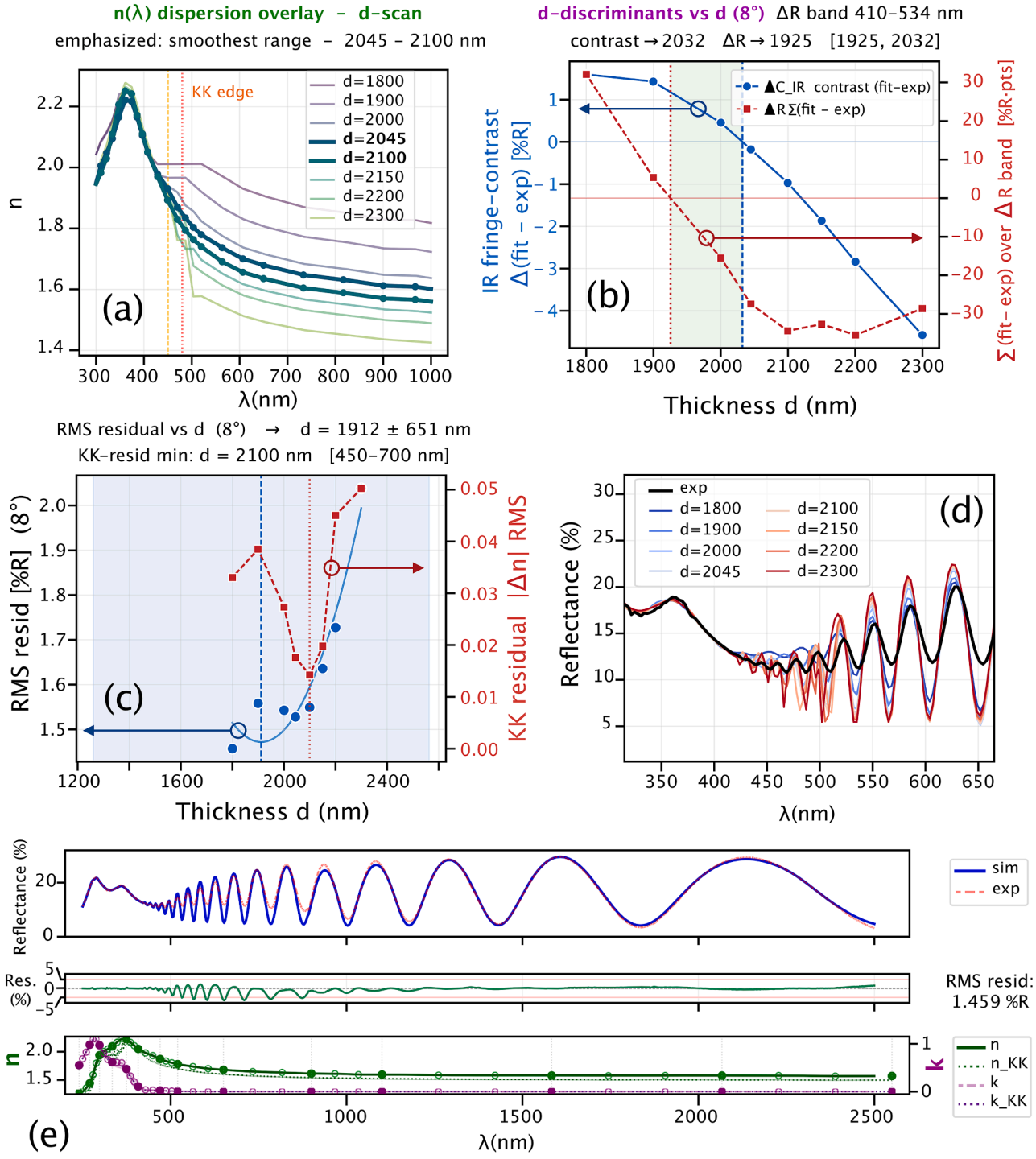


Fig. 8. ***d*-scan analysis, (a) through (d), for the sample in Fig. 6(b). The fitting results obtained using the optimal d_{fit} are also shown, (e). The solid blue curve in panel (c) is a parabolic fit to the RMS residuals, used to locate the most probable position of the minimum (and hence the effective thickness); it is not an eye guide. Magnified panels in full resolution are available in the supplementary material S2.**

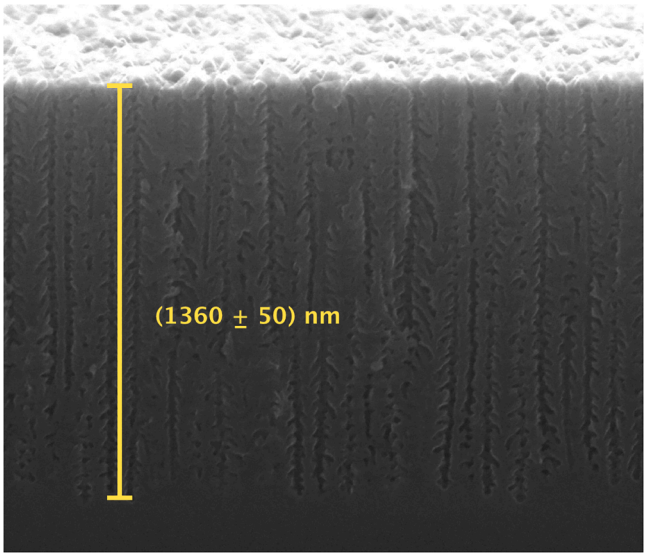


Fig. 9. SEM cross section of a low porosity PSi sample with rough interfaces.

will necessarily depend on the R_{exp} and R_{fit} curves and on their differences, can be evaluated to be no less than ± 30-50 nm for samples of $d = 1000$ nm.

As a validation of the *d*-scan approach, we would like to remark that for the SiO_2 sample described in section 4.1, the *d*-scan indicates a thickness of roughly (303 ± 3) nm, selected without any assumption on the refractive index: among the scanned thicknesses, ranging from 260 nm to 330 nm, it is the one that returns the most regular $n(\lambda)$ dispersion. That this thickness also yields the correct SiO_2 index is a validation of the criterion, consistent with the role, maintained throughout this work, of the dispersion regularity as the primary and most reliable indicator, more robust than the reflectance residual, which on this low-contrast film is nearly insensitive to thickness.

4.2.2. d_{eff} from flat-interface homogeneous samples with medium and high porosity

To test the validity of the proposed approach, we tested the *d*-scan method with samples with flat interfaces whose SEM thickness was also measured. Both samples described here were fabricated on n^+ Si, 3-7 mΩ·cm, phosphorus-doped, (100) oriented Si substrate using an electrochemical solution whose composition was HF(50%) and EtOH in a 3:7 proportion V/V. The etching current was 75 mA/cm^2 for the medium porosity sample and 333 mA/cm^2 for the high porosity sample. These parameters give a 55% and 75% average porosity. The SEM cross section of these sample is shown in Fig. 6 (a) and (b), respectively.

The *d*-scan analysis for the medium porosity sample is shown in Fig. 7 (a)-(d) and the fitting obtained using the optimal d_{eff} is shown in Fig. 7 (e). It's interesting to note that while the SEM-measured thickness is within the range suggested by whole set of *d*-scan parameters, the analysis of the *n* dispersion curves in (a) is the most precise and indicate the same *d* value as the SEM cross section. This confirms the optimal homogeneity of the porous layer and the flatness of the interfaces, that are the main parameter leading to $d_{eff} = d_{SEM}$.

Medium porosity samples are the easier kind of samples, but high porosity samples constitute a significantly harder task since the EMA models in that region show the larger differences (see Fig. 1). The high porosity samples have also been repeatedly reported as challenging samples in scientific literature not only for the EMA models difference but also for the onset of scattering phenomena [36,63]. For this reason, testing the proposed model using Ophira on the spectra of high-porosity samples is an important validation test. The SEM cross section of the high porosity sample is shown in Fig. 6 (b) In Fig. 8 we show the same analysis performed in Fig. 7 for the medium porosity sample. Panels from (a) to (d) show the d-scan analysis and panel (e) shows the best fit using d_{eff} within the optimal range. Although the analysis shows that the fit quality decreases for the fringes amplitude, the fringes position remains well fitted, and the amplitude has no effect on the determination of the refractive index. The *d*-scan analysis again determines that d_{eff} is also in this case equal to d_{SEM}, confirming that the porosity does not affect the quality of the information delivered by the *d*-scan and that the comparison of the *n* dispersion curves is, within the *d*-scan parameters, the most stable.

We performed many tests with different samples and we also observed that Ophira *d*-scan is more reliable than just maxima position when it comes to the analysis of thin samples where there are only 1-2 maxima within the IR transparency windows, since it relies much less on the fringes positions but more on the overall fitting behavior.

4.2.3. d_{eff} from thick- or rough-interface samples, low porosity

The coincidence between d_{eff} and d_{SEM} fails when the sample, as we discussed earlier, is inhomogeneous, has rough interfaces or both. In those cases, the light will see an effective refractive index that can be larger or smaller than the local measurement by SEM depending on the sample's inhomogeneities and overall shape. As an example, here is a low porosity PSi sample with inhomogeneities on both interfaces. In Fig. 9 is shown the SEM cross section of the sample, where the roughness of the top and bottom interfaces is clearly visible. With respect to the samples analyzed in the previous paragraph also the error on the SEM thickness is significantly higher.

The results of the *d*-scan analysis are shown in Fig. 10 (a) to (d). In the same figure, panel (e) shows the fit for a thickness within the d-scan optimal fitting range, while in panel (f) is shown the best fit obtained using $d_{fit} = d_{SEM}$. It is easy to see that the fit in (f) is in no way the possible correct simulation of the experimental reflectivity spectrum, while the simulation in (e) is significantly better. Since d_{eff} is not a geometrical thickness but is the thickness that better comply with the optical response (see 2.5), therefore in a sample with rough interfaces as this one d_{eff} is defined with an uncertainty that roughly is $\Delta d_{eff} \geq 50$ nm. This difference illustrates and demonstrates how the effective optical response of a complex and rough material can differ from the one that can be calculated using the physical thickness obtained from reliable microscopy tools. Please note that using d_{SEM} the refractive index is the one of a low porosity sample as the sample clearly is and can be seen in its SEM cross section in Fig. 9. However, the sample behaves optically as a sample with a medium porosity and a smaller effective refractive index.

A further interesting comparison can be obtained by comparing the KK-residues as shown in Fig. 11. In panels (a) and (b), relative to $d_{fit} = 1800$ nm and $d_{fit} = 1900$ nm, respectively. There is no significant difference between the two residues, indicating the factual uncertainty in the determination of d_{eff} on samples with very thick interfaces. However, panel (c) shows residues for $d_{fit} = d_{SEM} = 1350$ nm, where the residues increase and the overall shape is significantly different from the calculated n_{KK}, certifying the weaker physical significance of the fitting obtained using the physical porous layer thickness. Quantitatively, RMS/σ is 2.8 and 4.0 at $d_{fit} = 1800$ and 1900 nm (Fig. 11a,b), near the significance threshold of about three, whereas at $d_{fit} = d_{SEM} = 1350$ nm (Fig. 11c) it reaches 8.4, a clear inconsistency accompanied by a visibly distorted dispersion.

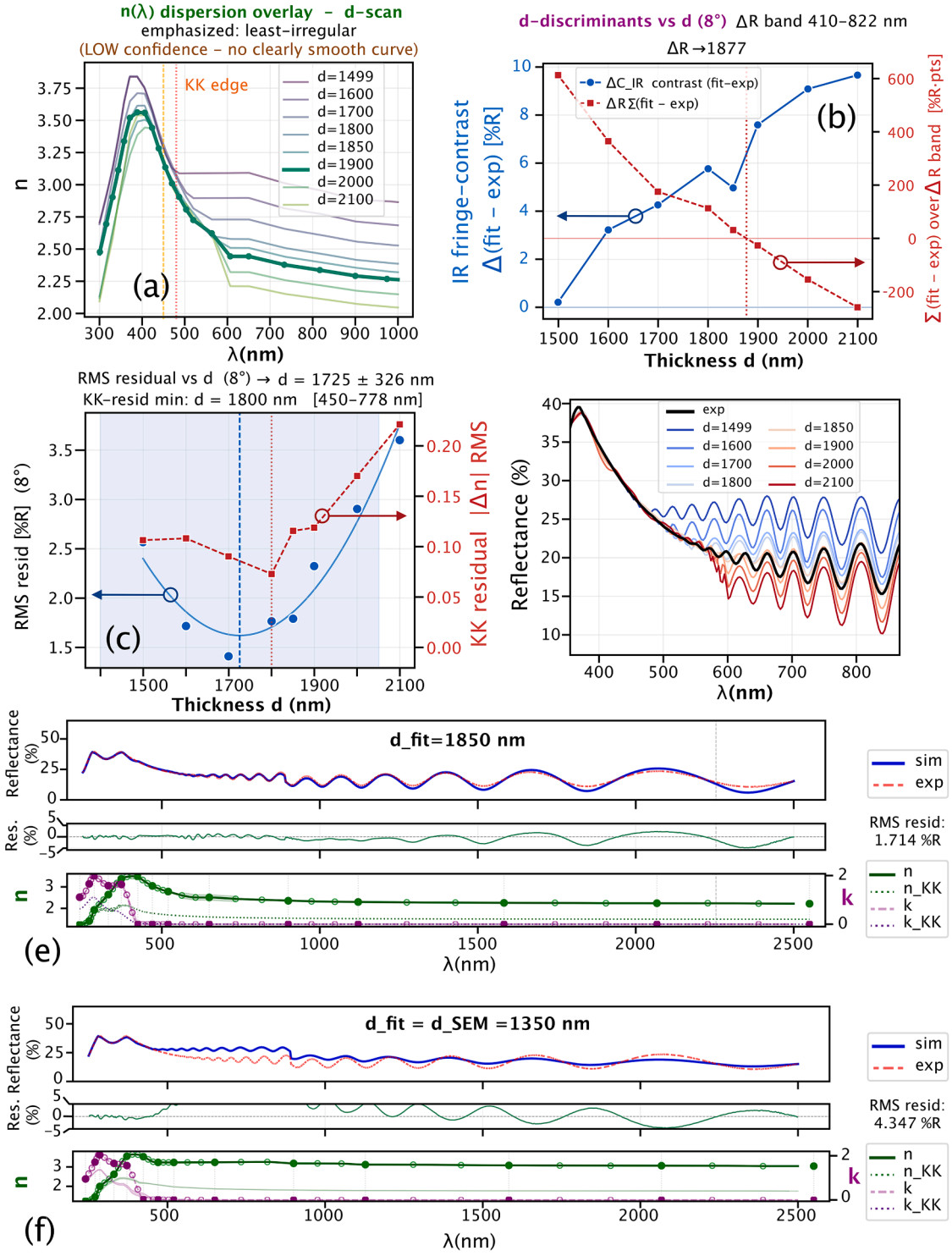


Fig. 10. ***d***-scan analysis, (a) through (d), for the sample in Fig. 9. The fitting results obtained using the optimal fitting are also shown, (e), while the fit obtained using the SEM thickness is shown in (f). The solid blue curve in panel (c) is a parabolic fit to the RMS residuals, used to locate the most probable position of the minimum (and hence the effective thickness); it is not an eye guide. Magnified panels in full resolution are available in the supplementary material S3.

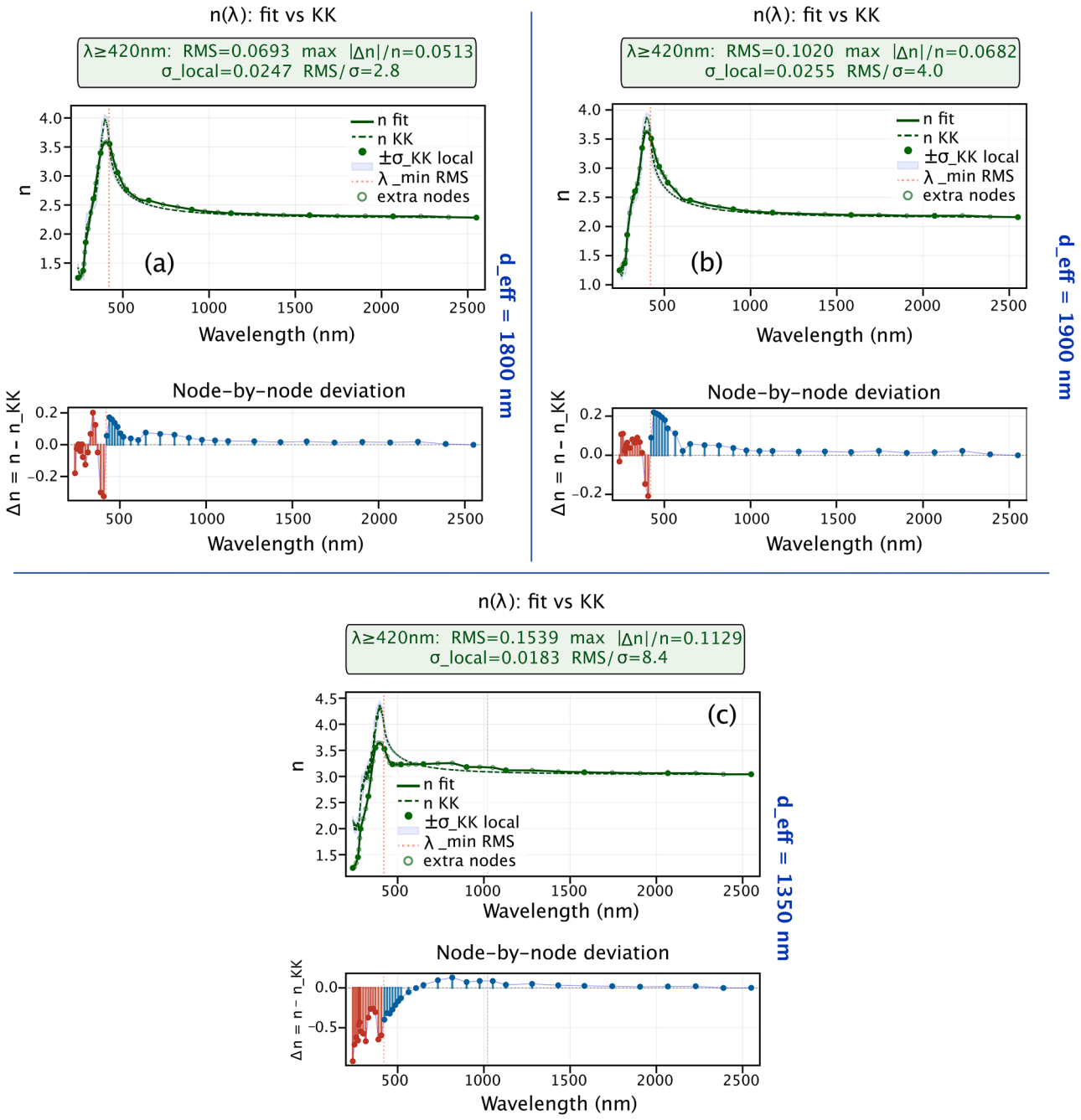


Fig. 11. Comparison of the KK residues for three different d_{eff} values. In (a) and (b) the KK residues are quite similar, while in (c), when $d_{eff} = d_{SEM}$, the residues and the shape of the fitted n dispersion curve is dramatically different from the calculated n_{KK}. Magnified panels in full resolution are available in the supplementary material S4.

4.3. Comparison with industry-standard tool

The last step in validating the method and its transposition in the Ophira code is the comparison of the Ophira fitting with standard state-of-the-art commercial fitting tools as is the Scout software. In Fig. 12 is shown the comparison of Ophira and Scout fitting of the medium porosity sample we already discussed in § 4.2.2. In (a) there is the fitting of the pristine sample, while in (b) there is the fitting after the electrochemical Er impregnation of the sample, whose optical results were previously published [64,65] and are reproduced here with Scout. Both spectra are taken at 8° of incidence. The information retrieved with both tools is fully equivalent in terms of reflectivity simulation, d_{eff} and n-dispersion curve. There is a difference in k-dispersion curve, but since for both tools the fitting is not fully superposed to the sample experimental spectrum, therefore these small values are the mathematical algorithm strategy to compensate for the differences. Please note however that the fact that Ophira is not bound to an oscillator-based methods lead to a noisier but flatter dispersion curve for k. Another important comment on this comparison: it was impossible to obtain such a high-quality fitting without adding oscillators to the Scout model.

The complexity of the porous structure, already discussed, implies that a simple model is insufficient for an optimal fitting of the reflectivity spectra. The consequences is that while with Ophira there is no specific oscillator model and the uncertainty is found in the excellent but imperfect adhesion to KK calculated dispersion curves, using the model-based software the uncertainty is hidden behind a perfect KK-

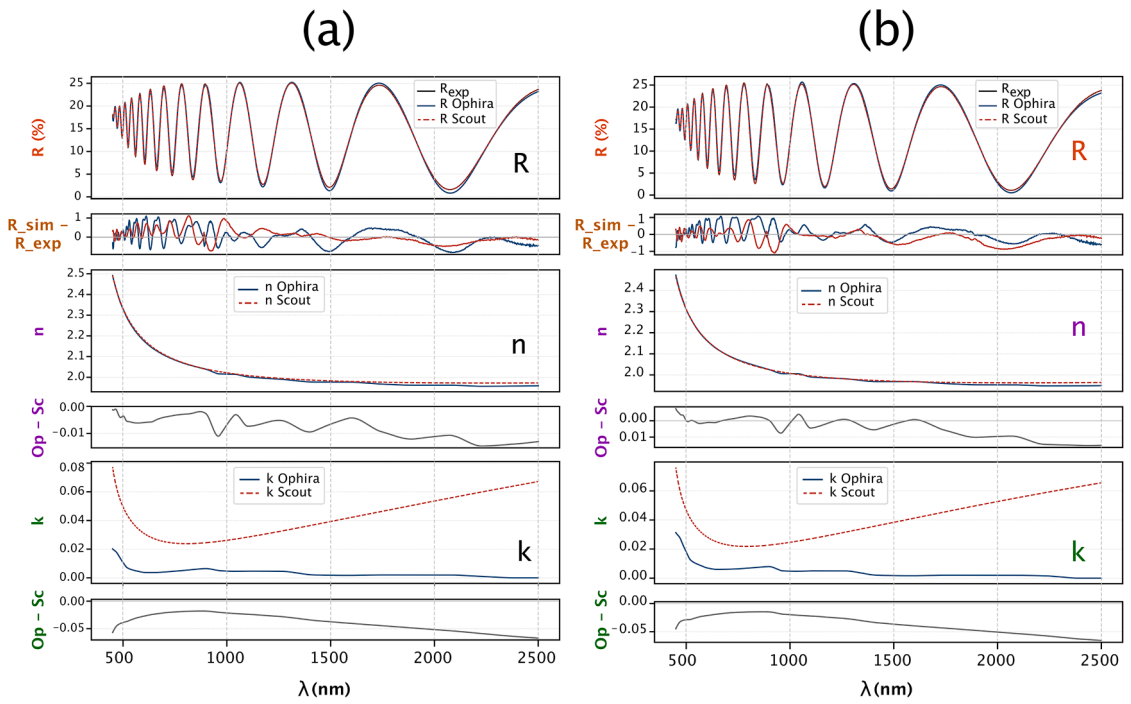


Fig. 12. Comparison of Scout and Ophira fitting on a pristine (a) and Er-filled (b) medium-porosity sample with a $d_{SEM} = 1300$ nm. The spectra are measured at 8° of incidence. The wavelength dispersion curves of n and k for the two tools are also reported. Magnified panels in full resolution are available in the supplementary material S5.

Table 2
Refractive index retrieved by Ophira and by Scout for the medium-porosity sample of §4.2.2 before and after erbium infiltration, at three reference wavelengths. The layer thickness is held fixed at $d = 1325$ nm between the two states, so that Δn reflects only the change of the refractive index. Both tools retrieve a negative change of comparable magnitude, agreeing to within about 0.005 across the individual wavelengths and to 0.003 in the spectral mean.

λ (nm)	n Ophira (pristine)	n Ophira (Er)	Δn Ophira	n Scout (pristine)	n Scout (Er)	Δn Scout
1000	2.015	2.006	−0.009	2.021	2.007	−0.014
1400	1.977	1.969	−0.009	1.987	1.974	−0.013
2000	1.962	1.953	−0.009	1.973	1.963	−0.010
mean 450–2500			−0.010			−0.013

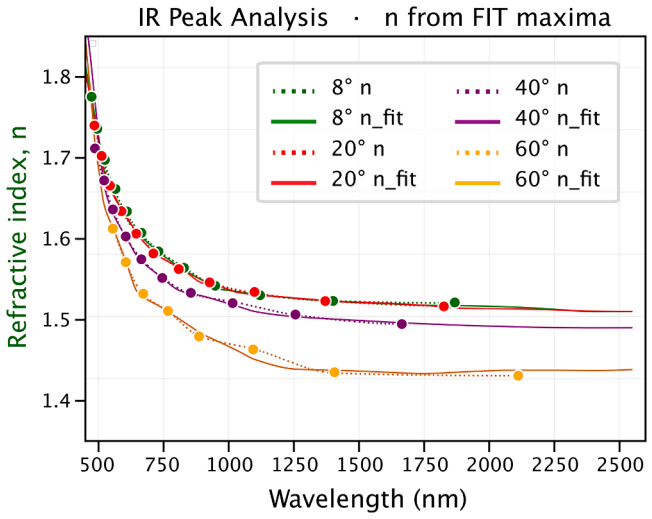


Fig. 13. Effective refractive index modification with the increase of the incidence angle from 8° to 60°. The sample is the twin of the sample whose results have been published in G. Mula et al. [50], Fig. 10(b). In the caption n_fit is the refractive index dispersion calculated from the fitting procedure, while n is the dispersion curve obtained from the maxima position. The maxima positions are visible as the dots on the n dispersion curves. The plot is one of the possible outputs from Ophira.

consistency, a difficult to explain choice of the oscillators and a still imperfect superposition of R_{sim} and R_{exp}. On the other side, both approaches retrieve a fully reliable optical response that maintains its full physical meaning.

A further important observation comes from Fig. 12, panel (b). In that panel is shown the analysis of the same sample of panel (a) after a process of Er electrochemical infiltration. Both tools are able to detect the small refractive index modification in the sample, and the results are summarized in Table 2. Both software detect a small but reliable blueshift and the average Δn is of the same order. This confirms the validity of the model and of the Ophira implementation against stable and worldwide recognized tools as Scout software.

4.4. Multi-angle analysis and birefringence

The multiangle fitting allows the user to track the vertical behavior of the refractive index within the layer. While Ophira is clearly unable, in its present development form, to resolve the ordinary and extraordinary index in a birefringent behavior, the modification of the effective refractive index n_{eff} will give useful information on the sign and relative magnitude of the birefringence in a given sample if the optical axis is vertical [50].

The Ophira analysis is shown in Fig. 13, where the dispersion curves of n_{eff} for the different incidence angles are shown. The thickness used here is the SEM thickness value, that within the fitting uncertainty coicides with Ophira d-scan analysis. Using the same value for d, the

dotted lines represent the dispersion curves obtained by the position of the interference maxima (visible as the dots on the curves), taking into account the incidence angle, while the full lines are the Ophira-fitted refractive index dispersion curves. Each angle has the same color in the two modalities. At 1400 nm, the Δn is ≈ -0.09 for both methods. These values are therefore fully congruent with the published values on a twin sample and further confirm the physical soundness of Ophira and its validity in the determination of the optical parameters.

Please note that because $n(\lambda)$ is reconstructed from regularized free nodes rather than an analytic dispersion law, it is a robust, assumption-light estimate suited to routine characterization, at the cost of a mild non-smoothness where the data are least constraining. A KK-constrained parametric dispersion would yield a smoother curve but is a different, heavier tool; the two serve different purposes.

5. Conclusions

We propose an approach to extract the optical parameters from the reflectivity spectra of transparent complex thin films that does not rely on any EMA model, yet remains constrained by the physical coherence of the phenomena. The approach is implemented in the Ophira code, developed with PSi in mind, but the availability of the code allows a user to adapt the PSi-specific parameters to other materials. The KK consistency is computed after the fit and can be used to constrain the retrieval to physically sound solutions. This property underlies the d-scan tool, which identifies the effective thickness that reproduces the experimental spectrum from a single reflectivity measurement at normal or quasi-normal incidence. For homogeneous layers the optically deduced effective thickness coincides with the physical thickness, while for inhomogeneous or rough layers the two can differ in either direction, the effective thickness being the quantity the optics actually act upon.

The approach and the code have been validated on a simple reference material (SiO_2 on Si) and by comparison with Scout, a well-established commercial tool. The comparison shows that both tools are sensitive to small variations in the sample parameters, as demonstrated by the erbium-infiltration test. As a final check, Ophira independently reproduces a previously published birefringence result, and the negative sign of the birefringence is retrieved whether the thickness is taken from SEM or from the effective optical thickness.

Ophira is not intended as a replacement but as a companion to the available approaches and tools. Representing the refractive-index dispersion through nodes allows an intuitive handling of complex and diverse samples, and switching between samples of very different refractive index takes a matter of seconds. Where established commercial tools offer powerful but complex functionality that demands wider user expertise, for instance the choice among different EMA models, Ophira aims to be an intuitive, reliable and rapid tool that stays grounded in physics, suited to everyday analysis in a sample-fabrication laboratory.

List of abbreviations

Abbreviation	Definition
AI	artificial intelligence
DW	Debye–Waller
EMA	effective-medium approximation
EOT	effective optical thickness
EtOH	ethanol
HF	hydrofluoric acid
IR	infrared
KK	Kramers–Kronig
MSKK-1	multiply-subtractive Kramers–Kronig relation (one subtraction)
Ophira	OPtical tHIn-film Reflectance Analyzer
PbS	lead sulfide
PCHIP	piecewise cubic Hermite interpolating polynomial
PSi	porous silicon
RMS	root-mean-square
RMSE	root-mean-square error
SEM	scanning electron microscopy

(*continued on next column*)

(*continued*)

Nomenclature

Roman symbols

Symbol	Definition
d	layer thickness
d_{fit}	trial thickness scanned during the fit
d_{eff}	effective thickness retrieved from the optical fit
d_{SEM}	layer thickness measured from the SEM cross-section
E	photon energy
E_{IR}	infrared anchor energy (= 1240/2500 eV)
k, $k(\lambda)$	extinction coefficient and its dispersion
m	interference (fringe) order
N	number of spectral points
N_{f}	complex refractive index of the film
N_2	complex refractive index of the substrate
n, $n(\lambda)$	refractive index (real part) and its dispersion
n_{eff}	effective refractive index
n_{KK}	refractive index from the KK transform of k
R	reflectance
R_{exp}, R_{fit}, R_{sim}	measured, fitted, and simulated reflectance
$r_{ij}^{s,p}$	Fresnel amplitude reflection coefficients at interface ij (s, p polarization)
s, p	s- and p-polarization

Greek symbols

Symbol	Definition
Δn	$n - n_{\mathrm{KK}}$ (Kramers–Kronig residual)
ε_1, ε_2	real and imaginary parts of the dielectric function ($\varepsilon_2 = 2nk$)
θ_0, θ_1, θ_2	angle of incidence, refraction angle in the film, refraction angle in the substrate
λ	wavelength
σ_{local}	local standard deviation (intrinsic noise) of n_{KK}
φ	phase accumulated in one traversal of the film
φ_{norm}, φ_{foot}	normal-incidence and oblique-incidence ("foot") phase contributions

Other

Symbol	Definition
$\mathscr{P}$	Cauchy principal value
RMS($n - n_{\mathrm{KK}}$)	root-mean-square Kramers–Kronig-consistency residual
RMS/σ	Kramers–Kronig residual normalized by σ_{local}

Declaration of generative AI and AI-assisted technologies in the writing process

During the preparation of this work the author used Anthropic Claude (Opus 4.8) in order to assist with the description of the mathematical and methodological aspects of the software in the Methods section, and to check the consistency between the manuscript text, the reported declarations and the software. The remaining text is the author's own writing, revised in the light of the tool's comments and the author takes full responsibility for the content of the publication.

Funding

This research received no specific grant from funding agencies in the

public, commercial, or not-for-profit sectors.

Code availability

The Ophira software (v1.0.1) is released by the Università degli Studi di Cagliari under the PolyForm Noncommercial License 1.0.0, which permits any noncommercial use, including academic research and education, while commercial use is reserved to the rights holder. The source code is available at https://github.com/guidomula/ophira, and the archived release is deposited at Zenodo (https://doi.org/10.5281/zenodo.21495779). The repository includes the fitting engine, the user interface, and the accompanying documentation (user manual, physics and mathematics reference, and operating procedures).

Data availability

All data needed to support the conclusions are within the text and the figures. The original reflectance spectra files are available from the author upon reasonable request.

Declaration of competing interest

The author declares that he has no known competing financial interests or personal relationships that could have appeared to influence the work reported in this paper.

Acknowledgements

The author thanks Andrea Falqui (Università degli Studi di Milano Statale, Milano, Italy) and Luca Boarino, Eleonora Cara and Giuseppe Leonetti (Istituto Nazionale di Ricerca Metrologica, Torino, Italy) for providing the SEM cross-section images used as a thickness reference.

Supplementary materials

Supplementary material associated with this article can be found, in the online version, at doi:10.1016/j.tsf.2026.141059.

Appendix

Appendix A - Complex refraction angles. With complex indices, Snell's law conserves the tangential wavevector,

$$\sin\theta_0 = N_f \sin\theta_1 = N_2 \sin\theta_2,$$

and the film propagation cosine is taken on the branch with non-negative real part,

$$\cos\theta_1 = \sqrt{1 - \frac{\sin^2\theta_0}{N_f^2}},$$

its real part setting the propagating component and its imaginary part the evanescent decay.

Appendix B - Fresnel coefficients

For each interface ij the s- and p-polarized amplitude reflection coefficients are

$$r_{ij}^{s} = \frac{N_i\cos\theta_i - N_j\cos\theta_j}{N_i\cos\theta_i + N_j\cos\theta_j}, \qquad r_{ij}^{p} = \frac{N_j\cos\theta_i - N_i\cos\theta_j}{N_j\cos\theta_i + N_i\cos\theta_j},$$

with s the field perpendicular and p the field parallel to the plane of incidence, and $i, j \in \{0, 1, 2\}$ labelling air, film and substrate.

Data availability

Data will be made available on request.

References

[1] SENSOFAR Metrology, 3D optical Profiler, (n.d.). https://www.sensofar.com/metrology/industry-research/sneox/(accessed July 9, 2026).
[2] KLA, KLA industrial thickness measurement tool, (n.d.). https://www.kla.com/products/instruments/thin-film-reflectometers/filmetrics-f10-ar/(accessed July 9, 2026).
[3] M.J. Sailor, Porous Silicon in Practice: Preparation, Characterization and Applications, Wiley-VCH, Weinheim, 2011, https://doi.org/10.1002/9783527641901.
[4] S. Setzu, S. Salis, V. Demontis, A. Salis, M. Monduzzi, G. Mula, Porous silicon-based potentiometric biosensor for triglycerides, Phys. Status Solidi A 204 (2007) 1434–1438, https://doi.org/10.1002/pssa.200674378.
[5] V.S.Y. Lin, K. Motesharei, K.P.S. Dancil, M.J. Sailor, M.R. Ghadiri, A porous silicon-based optical interferometric biosensor, Science 278 (1997) 840–843, https://doi.org/10.1126/science.278.5339.840.
[6] S. Dhanekar, S. Jain, Porous silicon biosensor: current status, Biosens. Bioelectron. 41 (2013) 54–64, https://doi.org/10.1016/j.bios.2012.09.045.
[7] N. Massad-Ivanir, G. Shtenberg, N. Raz, C. Gazenbeek, D. Budding, M.P. Bos, E. Segal, Porous silicon-based biosensors: towards real-time optical detection of target bacteria in the food industry, Sci. Rep. 6 (2016) 38099, https://doi.org/10.1038/srep38099.
[8] D.W. Boeringer, R. Tsu, Lateral photovoltaic effect in porous silicon, Appl. Phys. Lett. 65 (1994) 2332, https://doi.org/10.1063/1.112733.
[9] A.N. Parbukov, S.C. Bayliss, B. Unal, Photovoltaic properties of a novel stain etched porous silicon and its application in photosensitive devices, Opt. Mater. 17 (2001) 79–82.
[10] M. Tiddia, G. Mula, M. Mascia, E. Sechi, A. Vacca, Porous silicon–polyaniline hybrid composites synthesized through electroreduction of an aryldiazonium salt: preparation and photocurrent properties, RSC Adv. 6 (2016) 101880–101887, https://doi.org/10.1039/C6RA19868F.
[11] A. Pinna, F. Simbula, D. Marongiu, A. Pezzella, M. d'Ischia, G. Mula, Boosting, probing and switching-off visible light-induced photocurrents in eumelanin-porous silicon hybrids, RSC Adv. 5 (2015) 56704–56710, https://doi.org/10.1039/C5RA08605A.
[12] P. Granitzer, K. Rumpf, Filling of porous silicon with magnetic materials, Semicond. Sci. Technol. 31 (2015), https://doi.org/10.1088/0268-1242/31/1/014004.
[13] K. Rumpf, P. Granitzer, H. Michor, Porous silicon nanocomposites with combined hard and soft magnetic properties, Nanoscale Res. Lett. 11 (2016) 398, https://doi.org/10.1186/s11671-016-1617-0.
[14] P. Granitzer, K. Rumpf, P. Poelt, M. Reissner, Magnetic characteristics of Ni-filled luminescent porous silicon, Front. Chem. 7 (2019) 1–6, https://doi.org/10.3389/fchem.2019.00041.
[15] S.L. Tao, T.A. Desai, Microfabricated drug delivery systems: from particles to pores, Adv. Drug Delivery Rev. 55 (2003) 315–328, https://doi.org/10.1016/S0169-409X(02)00227-2.
[16] E. Anglin, L. Cheng, W. Freeman, M. Sailor, Porous silicon in drug delivery devices and materials, Adv. Drug Delivery Rev. 60 (2008) 1266–1277, https://doi.org/10.1016/j.addr.2008.03.017.

[17] W. Li, Z. Liu, F. Fontana, Y. Ding, D. Liu, J.T. Hirvonen, H.A. Santos, Tailoring porous silicon for biomedical applications: from drug delivery to cancer immunotherapy, Adv. Mater. 30 (2018) 1703740, https://doi.org/10.1002/adma.201703740.
[18] C.F. Wang, E.M. Mäkilä, M.H. Kaasalainen, M.V. Hagström, J.J. Salonen, J. T. Hirvonen, H.A. Santos, Dual-drug delivery by porous silicon nanoparticles for improved cellular uptake, sustained release, and combination therapy, Acta Biomater. 16 (2015) 206–214, https://doi.org/10.1016/j.actbio.2015.01.021.
[19] P. Ferrand, S. Setzu, R. Romestain, Photonic bandgap properties of nanoporous silicon microstructures, Eur. Phys. J. AP 16 (2001) 31–35.
[20] S. Setzu, P. Ferrand, R. Romestain, Optical properties of multilayered porous silicon, Mater. Sci. Eng. B 69–70 (2000) 34–42, https://doi.org/10.1016/S0921-5107(99)00261-5.
[21] S.Y. Choi, M. Mamak, G. von Freymann, N. Chopra, G.A. Ozin, Mesoporous Bragg stack color tunable sensors, Nano Lett. 6 (2006) 2456–2461. http://pubs.acs.org/doi/abs/10.1021/nl061580m.
[22] I. Ivanov, V. Skryshevsky, Porous silicon optical distributed Bragg reflector sensor: methods of characterization, in: 2020 IEEE 40th International Conference on Electronics and Nanotechnology (ELNANO), IEEE, Kyiv, Ukraine, 2020, pp. 327–330, https://doi.org/10.1109/ELNANO50318.2020.9088823.
[23] N. Ishikura, M. Fujii, K. Nishida, S. Hayashi, J. Diener, M. Mizuhata, S. Deki, Broadband rugate filters based on porous silicon, Opt. Mater. (Amst) 31 (2008) 102–105, https://doi.org/10.1016/j.optmat.2008.01.016.
[24] S. Ciampi, T. Böcking, K.A. Kilian, J.B. Harper, J.J. Gooding, Click chemistry in mesoporous materials: functionalization of porous silicon rugate filters, Langmuir 24 (2008) 5888–5892, https://doi.org/10.1021/la800435d.
[25] M.J. Sailor, Color me sensitive: amplification and discrimination in photonic silicon nanostructures, ACS. Nano 1 (2007) 248–252, https://doi.org/10.1021/nn700340u.
[26] D.N. Kumar, G. Shtenberg, R.S. Keri, Porous silicon-based biosensors for food safety and quality monitoring: a comprehensive review, Adv. Mater. Technol. 11 (2026) e71149, https://doi.org/10.1002/admt.71149.
[27] G. Rong, J.D. Ryckman, R.L. Mernaugh, S.M. Weiss, Label-free porous silicon membrane waveguide for DNA sensing, Appl. Phys. Lett. 93 (2008) 161109, https://doi.org/10.1063/1.3005620.
[28] P. Sharma, J. Harberts, R. Sánchez-Salcedo, P. Dehghankelishadi, N.H. Voelcker, Implantable, Label-Free NIR-based porous silicon biosensor for monitoring biomarkers in interstitial fluid, Adv. Sens. Res. 4 (2025) e00007, https://doi.org/10.1002/adsr.202500007.
[29] M. Yaghoubi, F. Rahimi, B. Negahdari, A.H. Rezayan, A. Shafiekhani, A lectin-coupled porous silicon-based biosensor: label-free optical detection of bacteria in a real-time mode, Sci. Rep. 10 (2020) 16017, https://doi.org/10.1038/s41598-020-72457-x.
[30] R. Vercauteren, C. Gevers, J. Mahillon, L.A. Francis, Design of a porous silicon biosensor: characterization, modeling, and application to the indirect detection of bacteria, Biosensors (Basel) 14 (2024) 104, https://doi.org/10.3390/bios14020104.
[31] C. Gevers, L. Lejeune, E. Masarweh, S. Hermans, L.A. Francis, Freestanding porous silicon membranes for sensing enabled by flow-through decoration of gold nanoparticles, ACS. Appl. Nano Mater. 8 (2025) 21285–21293, https://doi.org/10.1021/acsanm.5c03632.
[32] F.K. Başak, Noise-reduced optical detection of miRNA-155 by porous silicon through Morlet wavelet phase analysis, Biosens. Bioelectron. X 29 (2026) 100752, https://doi.org/10.1016/j.biosx.2026.100752.
[33] D.A.G. Bruggeman, Berechnung verschiedener physikalischer Konstanten von heterogenen Substanzen. I. Dielektrizitätskonstanten und Leitfähigkeiten der Mischkörper aus isotropen Substanzen (calculation of various physics constants in heterogeneous substances. I. Dielectricity constants and conductivity of mixed bodies from isotropic substances), Ann. Phys. 416 (1935) 636–664, https://doi.org/10.1002/andp.19354160705.
[34] D. Stroud, The effective medium approximations: some recent developments, Superlattices. Microstruct. 23 (1998) 567–573, https://doi.org/10.1006/spmi.1997.0524.
[35] J.C. Maxwell-Garnett, Colours in Metal Glasses and Metallic Films, Philos. Trans. R. Soc. Lond. A 203 (1904) 385–420.
[36] W. Theiß, Optical properties of porous silicon, Surf. Sci. Rep. 29 (1997) 91–192, https://doi.org/10.1016/S0167-5729(96)00012-X.
[37] T.H. Fung, T. Veeken, D. Payne, B. Veettil, A. Polman, M. Abbott, Application and validity of the effective medium approximation to the optical properties of nano-textured silicon coated with a dielectric layer, Opt. Express. 27 (2019) 38645, https://doi.org/10.1364/OE.27.038645.
[38] M. Khardani, M. Bouaïcha, B. Bessaïs, Bruggeman effective medium approach for modelling optical properties of porous silicon: comparison with experiment, Physica Status Solidi C 4 (2007) 1986–1990, https://doi.org/10.1002/pssc.200674420.
[39] J. Brandt, G. Dittrich, M. Thelen, H. Renner, P. Huber, M. Eich, A. Petrov, On the applicability of the Maxwell Garnett effective medium model to media with a high density of cylindrical pores, Opt. Mater. Express 14 (2024) 871, https://doi.org/10.1364/OME.516125.
[40] G. Mula, M.N. Akhtar, F.A. Pisu, G. Leonetti, B. Torre, L. Boarino, E. Cara, Si wafers unpredictable inhomogeneities and their crucial role in porous Si fabrication, Sci. Rep. 16 (2026) 17667, https://doi.org/10.1038/s41598-026-48737-3.
[41] F. Ferrieu, A. Halimaoui, D. Bensahel, Optical characterisation of porous silicon layers by spectrometric ellipsometry in the 1.5–5 eV range, Solid. State Commun. 84 (1992) 293–296, https://doi.org/10.1016/0038-1098(92)90124-R.
[42] N. Künzner, J. Diener, E. Gross, D. Kovalev, V.Y. Timoshenko, M. Fujii, Form birefringence of anisotropically nanostructured silicon, Phys. Rev. B Condens. Matter. Mater. Phys. 71 (2005) 1–8, https://doi.org/10.1103/PhysRevB.71.195304.
[43] S. Shichi, M. Fujii, T. Nishida, H. Yasuda, K. Imakita, S. Hayashi, Three-dimensional structure of (110) porous silicon with in-plane optical birefringence, J. Appl. Phys. 111 (2012) 084303, https://doi.org/10.1063/1.3703522.
[44] A.I. Efimova, E.Y. Krutkova, L.A. Golovan', M.A. Fomenko, P.K. Kashkarov, V. Y. Timoshenko, Birefringence and anisotropic optical absorption in porous silicon, J. Exp. Theor. Phys. 105 (2007) 599–609, https://doi.org/10.1134/S1063776107090178.
[45] L.A. Golovan, D.A. Ivanov, V.A. Melnikov, V.Y. Timoshenko, A.M. Zheltikov, P. K. Kashkarov, G.I. Petrov, V.V. Yakovlev, Form birefringence of oxidized porous silicon, Appl. Phys. Lett. 88 (2006) 2006–2008, https://doi.org/10.1063/1.2212534.
[46] J. Álvarez, P. Bettotti, I. Suárez, N. Kumar, D. Hill, V. Chirvony, L. Pavesi, J. Martínez-Pastor, Birefringent porous silicon membranes for optical sensing, Opt. Express. 19 (2011) 26106, https://doi.org/10.1364/oe.19.026106.
[47] I. Mihalcescu, G. Lerondel, R. Romestain, Porous silicon anisotropy investigated by guided light, Thin. Solid. Films. 297 (1997) 245–249, https://doi.org/10.1016/S0040-6090(96)09483-7.
[48] C.F. Ramirez-Gutierrez, I.A. Lujan-Cabrera, C. Isaza, E.K. Anaya Rivera, M. E. Rodriguez-Garcia, In situ photoacoustic study of optical properties of P-Type (111) porous silicon thin films, Nanomaterials 11 (2021) 1314, https://doi.org/10.3390/nano11051314.
[49] A.S. Fedorov, A.S. Teplinskaia, Thermal properties of porous silicon nanomaterials, Materials 15 (2022) 8678, https://doi.org/10.3390/ma15238678.
[50] G. Mula, M.N. Akhtar, F.A. Pisu, S. Bastide, A. Angelini, M. Rosero-Realpe, L. Boarino, Dramatic changes induced on porous silicon birefringence by shape-dependent properties, Sci. Rep. 16 (2026) 15198, https://doi.org/10.1038/s41598-026-41405-6.
[51] Wolfgang Theiss, Scout Home Page, Simon Theiss, Eitorf, Germany. https://mtheiss.com (accessed October 26, 2026).
[52] Wolfgang Theiss, Scout Technical Manual, Simon Theiss, Eitorf, Germany, https://www.mtheiss.com/help/final/pdf/scout3.pdf (accessed October 26, 2026).
[53] A. Kuzmenko, Kramers-Kronig constrained variational analysis of optical spectra, Rev. Sci. Instrum. 76 (2005) 083108, https://doi.org/10.1063/1.1979470.
[54] B. Johs, J.S. Hale, Dielectric function representation by B-splines, Phys. Status Solidi A 205 (2008) 715–719, https://doi.org/10.1002/pssa.200777754.
[55] B. Fodor, E. Agocs, B. Bardet, T. Defforge, F. Cayrel, D. Alquier, M. Fried, G. Gautier, P. Petrik, Porosity and thickness characterization of porous Si and oxidized porous Si layers – An ultraviolet–visible–mid infrared ellipsometry study, Microporous Mesoporous Mater. 227 (2016) 112–120, https://doi.org/10.1016/j.micromeso.2016.02.039.
[56] F. Aliabadi, F. Rahimi, A. Abouei Mehrizi, M. Nikkhah, S.S. Mohseni, F. Asghari, rHuEPO-α biosensing by porous silicon integrated into microchannels via reflectometric interference Fourier transform spectroscopy, Anal. Chem. 97 (2025) 11394–11401, https://doi.org/10.1021/acs.analchem.4c04693.
[57] C. Pacholski, M. Sartor, M.J. Sailor, F. Cunin, G.M. Miskelly, Biosensing using porous silicon double-layer interferometers: reflective interferometric Fourier transform spectroscopy, J. Am. Chem. Soc. 127 (2005) 11636–11645, https://doi.org/10.1021/ja0511671.
[58] K. Awawdeh, M.A. Buttkewitz, J. Bahnemann, E. Segal, Enhancing the performance of porous silicon biosensors: the interplay of nanostructure design and microfluidic integration, Microsyst. Nanoeng. 10 (2024) 100, https://doi.org/10.1038/s41378-024-00738-w.
[59] K.-S. Mun, S.D. Alvarez, W.-Y. Choi, M.J. Sailor, A. Stable, Label-free optical interferometric biosensor based on TiO2 nanotube arrays, ACS. Nano 4 (2010) 2070–2076, https://doi.org/10.1021/nn901312f.
[60] M. Born, E. Wolf, Principles of Optics, 7th (expanded) ed., Cambridge University Press, Cambridge, 1999 https://doi.org/10.1017/CBO9781139644181.
[61] O.S. Heavens, Optical properties of thin films, Rep. Prog. Phys. 23 (1960) 301, https://doi.org/10.1088/0034-4885/23/1/301.
[62] H.A. Macleod, Thin-Film Optical Filters, 4th ed., CRC Press, Boca Raton, 2010 https://doi.org/10.1201/9781420073034.
[63] A.E. Pap, K. Kordás, J. Vähäkangas, A. Uusimäki, S. Leppävuori, L. Pilon, S. Szatmári, Optical properties of porous silicon. part iii: comparison of experimental and theoretical results, Opt. Mater. (Amst) 28 (2006) 506–513, https://doi.org/10.1016/j.optmat.2005.02.006.
[64] G. Mula, T. Printemps, C. Licitra, E. Sogne, F. D'Acapito, N. Gambacorti, N. Sestu, M. Saba, E. Pinna, D. Chiriu, P.C. Ricci, A. Casu, F. Quochi, A. Mura, G. Bongiovanni, A. Falqui, Doping porous silicon with erbium: pores filling as a method to limit the Er-clustering effects and increasing its light emission, Sci. Rep. 7 (2017) 5957, https://doi.org/10.1038/s41598-017-06567-4.
[65] G. Mula, G. Manunza, S. Setzu, R. Ruffilli, A. Falqui, Characterization of Er in Porous Si, Nanoscale Res. Lett. 7 (2012) 376, https://doi.org/10.1186/1556-276X-7-376.